J. Fluid Mech. (2022), *vol*. 941, A3, doi:10.1017/jfm.2022.316

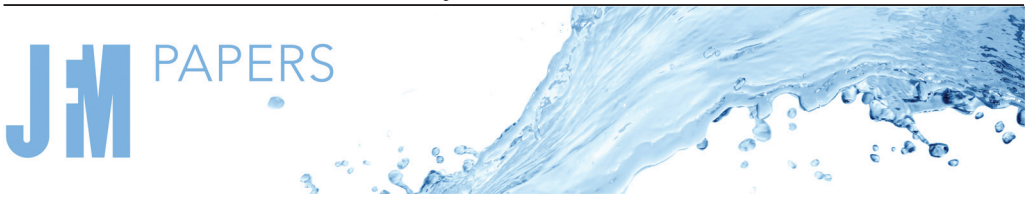

Objective momentum barriers in wall turbulence

Nikolas O. Aksamit[1,2,†] **and George Haller**[1]

[1]Institute for Mechanical Systems, Swiss Federal Institute of Technology, 8092 Zurich, Switzerland

[2]School of Earth and Environment, University of Canterbury, Christchurch 8140, New Zealand

(Received 16 December 2021; revised 25 February 2022; accepted 3 April 2022)

We use the recent frame-indifferent theory of diffusive momentum transport to identify internal barriers in wall-bounded turbulence. Formed by the invariant manifolds of the Laplacian of the velocity field, the barriers block the viscous part of the instantaneous momentum flux in the flow. We employ the level sets of single-trajectory Lagrangian diagnostic tools, the trajectory rotation average and trajectory stretching exponent, to approximate both vortical and internal wall-parallel momentum transport barrier (MTB) interfaces. These interfaces provide frame-indifferent alternatives to classic velocity-gradient-based vortices and high-shear boundaries between uniform momentum zones (UMZs). Indeed, we find that these elliptic manifold approximations and MTBs outperform standard vortices and UMZ interfaces in blocking diffusive momentum transport, which suggests our momentum barriers are physical features that may be the cause of coherence signatures in statistical and non-objective diagnostics. We also introduce normalized trajectory metrics that provide unprecedented visualizations of objective coherent structures by avoiding strong turbulence biases.

Key words: computational methods, turbulent boundary layers, vortex dynamics

1. Introduction

Early studies of turbulent boundary layer structures were fundamentally inspired by experimentally discovered structures, such as the streaks in boundary layers photographed by Kline *et al.* (1967) and the typical eddies forming large-scale motions described by Falco (1977), shown in figure 1. The pioneering bubble, fog and smoke experiments of the 1960s to 1980s (see, e.g. Fiedler & Head 1966; Kline *et al.* 1967; Offen & Kline 1974; Falco 1977; Bandyopadhyay 1980; Head & Bandyopadhyay 1981) quantified intermittent material features and boundary layer structures on which coherent structure identification methods continue to rely for validation.

† Email address for correspondence: nik.aksamit@canterbury.ac.nz

Figure 1. Material wall-bounded turbulent structures visualized with smoke. Reproduced from Falco (1977) with the permission of AIP Publishing.

Boundary layer tracer experiments suggest an organization of fluid by individual vortices at low Reynolds number (*Re*), and by packets or collections of vortices as turbulence increases. The 33°–45° angle at which individual vortices extend from the lower boundary has been recreated in multiple experiments for a variety of Reynolds numbers (Falco 1974; Bandyopadhyay 1980; Head & Bandyopadhyay 1981). The diameter of vortex heads has been found to be a fraction of the boundary layer height δ and scales inversely with *Re* from 0.01δ–0.2δ (Falco 1974, 1977). Typical vortices also appear to self-organize into bulges, or large scale motions, with streamwise extent ranging from 1.5–2.5δ (Falco 1977), which collectively rise at an inclination angle of 18°–20° (Bandyopadhyay 1980; Head & Bandyopadhyay 1981). In subsequent hot-wire and particle image velocimetry studies, these ranges of values have been recreated and expanded, but the original measures of material structures remain as the ground-truth for comparison (Adrian 2007).

Advances in experimental techniques and simulation provided highly resolved velocity fields that stimulated the development of quantitative criteria for the identification of structures seen in tracer experiments (Adrian 2007). Some of these criteria extract isosurfaces of velocity components to define uniform momentum zones (UMZs), while others employ diagnostic scalar fields, such as the Q-, λ_2-, Δ- and λ_{ci}-parameters, to define vortices (Hunt, Wray & Moin 1988; Jeong & Hussain 1995; Zhou *et al.* 1999; Adrian, Meinhart & Tomkins 2000*b*; Gao, Ortiz-Due ns & Longmire 2011). Yet other approaches identify a relevant temporal or spatial scale and employ a conditional averaging prior to feature extraction (see Dennis & Nickels 2011; Gul, Elsinga & Westerweel 2020).

UMZs were first documented in the early experimental study of Meinhart & Adrian (1995), leading to the seminal work of Adrian *et al.* (2000*b*) who suggested that wall-bounded turbulence may be described as a collection of layered zonal structures distinguished by their common streamwise velocities. These structures appear between rapid changes in streamwise velocity across strong shear regions where spanwise vorticity may be concentrated. The relevance of these jumps has been supported by analogous jumps in streamwise velocity at turbulent/non-turbulent interfaces and by nearby hairpin vortices and other vortical features. The core statistical methods used to make these inferences about UMZs and their boundaries were developed by Adrian *et al.* (2000*b*) with additional modifications proposed by De Silva, Hutchins & Marusic (2015), Eisma *et al.* (2015), Laskari *et al.* (2018), Fan *et al.* (2019) and others. With the help of these tools, UMZs have been investigated in a number of wall-bounded flows, including turbulent boundary layers, channel flows and pipe flows at various Reynolds numbers (Adrian *et al.* 2000*b*; Kwon *et al.* 2014; De Silva *et al.* 2015, 2017; Gul *et al.* 2020). UMZs have also been widely used as tools to validate other models (Saxton-Fox & McKeon 2017; Bautista *et al.*

2019) and generate descriptions of wall-turbulence organization (Adrian 2007; Hwang & Sung 2018).

Despite these advances, several practical issues are known with the currently used probability-based UMZ identification scheme, including its sensitivity to the size of the domain, to the number of velocity vectors used in identifying significant velocities (and thus extension to three-dimensional data) and to the number of bins used to reveal streamwise velocity peaks. Two more fundamental issues, however, also arise. First, the broadly hypothesized role of UMZs as fundamental turbulence-organizing zonal-like structures that influence the wall-transverse transport of streamwise linear momentum is often cited but has not yet been directly verified (e.g. Westerweel *et al.* 2009; Eisma *et al.* 2015; De Silva *et al.* 2017; Fan *et al.* 2019). While it is common for researchers to discuss these zonal-structures, and their probable physical importance, there is currently limited understanding of the momentum transport they induce (Montemuro *et al.* 2020). Nibbling, engulfment and entrainment are often studied as influential processes for mass and momentum flux, but fluxes through UMZ interfaces are typically estimated indirectly through conditional sampling and average Reynolds stress profiles. Second, the topology of streamwise velocity level sets (UMZ interfaces) is not objective, i.e. depends on the frame of reference of the observer. This is at odds with the tracer patterns arising in foundational tracer experiments (e.g. Kline *et al.* 1967; Falco 1977; Head & Bandyopadhyay 1981) that originally inspired the study of UMZs, given that those patterns are material and hence are inherently frame-indifferent. Additionally, level-set approaches that rely on Reynolds decompositions, including those in quadrant and octant analysis, introduce a non-physical distortion of the reference frame when different averages are subtracted from each grid cell (Adrian, Christensen & Liu 2000*a*; Kwon, Hutchins & Monty 2016; Saxton-Fox & McKeon 2017).

One might dismiss the concern about observer dependence by saying that a correct understanding of UMZs in the frame of the experiment is sufficient. The problem with this argument is that a description of features tied to material observations cannot be correct if it only holds in the current frame of observation, whether or not one ever intends to change that frame. More broadly speaking, truly unsteady flows may have convenient frames but have no distinguished frames, as already noted by Lugt (1979). This is the reason why objectivity (or indifference to Euclidean coordinate changes) as a litmus test for flow feature identification was already proposed in the 1970s (Drouot 1976; Drouot & Lucius 1976; Astarita 1979; Lugt 1979), prompting a number of recent approaches to adopt observer-indifference as a minimal requirement in coherent structure detection (see Haller 2005, 2015; Peacock, Froyland & Haller 2015; Kirwan 2016; Günther & Theisel 2018, for reviews).

Descriptions of experimentally observed vortical features within and surrounding UMZs (e.g. Head & Bandyopadhyay 1981) also face objectivity as a minimal self-consistency requirement. Yet the Q-, λ_2-, Δ- and λ_{ci}-isosurfaces used for this purpose are not objective and hence their predictions for observed material tracer patterns, or momentum transport blocking, cannot be accurate (see Haller 2005, 2021). While correlations may exist between measured scalar concentrations and the features of these non-objective diagnostics (e.g. Westerweel *et al.* 2009; Eisma, Westerweel & van de Water 2021), there can be no causal relationship. Several formal modifications of these vortex diagnostics have been proposed to make them objective, but only the approach of Liu, Gao & Liu (2019*a*); Liu *et al.* (2019*b*) would be generally applicable, as found by Haller (2021). Yet, for lack of a direct connection to material mixing and transport, even correct objectivizations of the currently used Q-, λ_2-, Δ- and λ_{ci}-procedures for vortex identification would depend on their users. Indeed, the users of these procedures are

expected to pick values for visualized isosurfaces based on their own expectations for the results (see, e.g. Dubief & Delcayre 2000). This commonly used approach results in a subjective view of the flow, as recently highlighted by Dong & Tian (2020).

In a parallel development, objective mathematical descriptions of long-term and short-term material deformation have lead to the notions of Lagrangian coherent structures (or LCS) and objective Eulerian coherent structures (or OECS) (see, e.g. Haller 2015; Serra *et al.* 2017; Beron-Vera *et al.* 2018; Serra *et al.* 2020). Some of these approaches have been used to identify vortices away from turbulent/non-turbulent interfaces (TNTIs) in gravity current experiments (Neamtu-Halic *et al.* 2019), as well as to look at boundary layer structures in PIV studies (Green, Rowley & Haller 2007; Pan, Wang & Zhang 2009; Wilson, Tutkun & Cal 2013; He *et al.* 2016; Eisma *et al.* 2021). LCSs and OECSs are, however, constructed as boundaries of coherent structures in passive tracer advection rather than minimizers of momentum transport, as would be required for a physical UMZ interface analogue.

Recently, Haller *et al.* (2020) developed a theory of objective material barriers for the transport of active vector fields, such as vorticity and momentum. These active barriers are sought as material surfaces that block an objectively defined transport of momentum or vorticity more than any other neighbouring material surface. Solving this optimization problem leads to an associated steady, three-dimensional (3-D), incompressible dynamical system (the barrier equation) whose structurally stable stream surfaces (invariant manifolds) are precisely the active transport barriers. Haller *et al.* (2020) showed how active versions of LCS diagnostics, such as the active finite-time Lyapunov exponents (aFTLE) and the active polar rotation angle (aPRA), provide previously unseen levels of detail for momentum-transport barriers in direct numerical simulations of a turbulent channel flow. Instantaneous limits of active material barriers can also be extract via the same machinery. The latter Eulerian barriers are objectively defined surfaces that block the instantaneous flux of the active vector field in question.

Here, we use this recent theory of instantaneous active barriers to define and visualize both momentum trapping vortices and momentum blocking internal interfaces (MTBs) objectively based on their broadly envisioned role as minimizers of momentum transport. To adapt the active barrier field methods to large datasets, and numerically identify large invariant manifolds of the active barrier equations, we use recently developed single-trajectory-based objective coherent structure diagnostics, the trajectory rotation average (TRA) and trajectory stretching exponent (TSE), from Haller, Aksamit & Bartos (2021). Combining these theories, we develop a simple, systematic procedure that visualizes both MTBs and momentum-trapping vortices in general 3-D, wall-bounded turbulence. We also show that the active-barrier-based approach developed here locates vortices and MTB interfaces with significantly lower viscous momentum flux than nearby surfaces obtained from the broadly used velocity-gradient-based vortex diagnostics and non-objective UMZ definition.

2. Methods

2.1. *Objective instantaneous barriers to momentum transport*

For a 3-D fluid velocity field $\boldsymbol{v}(\boldsymbol{x}, t)$ with density $\rho(\boldsymbol{x}, t)$, the equation of motion can be written as

$$\rho \frac{\mathrm{D}\boldsymbol{v}}{\mathrm{D}t} = -\nabla p + \nabla \cdot \boldsymbol{T}_{\mathrm{vis}} + \boldsymbol{q}, \tag{2.1}$$

where $\mathrm{D}/\mathrm{D}t$ is the material derivative, $p(\boldsymbol{x}, t)$ is the equilibrium pressure, $\boldsymbol{T}_{\mathrm{vis}}(\boldsymbol{x}, t)$ is the viscous stress tensor and $\boldsymbol{q}(\boldsymbol{x}, t)$ contains the external body forces. Fluid trajectories generated by the velocity field $\boldsymbol{v}$ are solutions, $\boldsymbol{x}(t; t_0, \boldsymbol{x}_0)$, of the ordinary differential equation $\dot{\boldsymbol{x}} = \boldsymbol{v}(\boldsymbol{x}, t)$ with initial position $\boldsymbol{x}_0$ at the initial time t_0. These fluid trajectories enable the definition of the flow map $\boldsymbol{F}_{t_0}^{t} : \boldsymbol{x}_0 \mapsto \boldsymbol{x}(t; t_0, \boldsymbol{x}_0)$. A material surface $\mathcal{M}(t)$ is then a two-dimensional (2-D) manifold,

$$\mathcal{M}(t) = \boldsymbol{F}_{t_0}^{t}[\mathcal{M}(t_0)], \tag{2.2}$$

evolving under the flow map from its initial position $\mathcal{M}(t_0)$.

To identify exceptional momentum-transport minimizing surfaces, we must first agree on a definition of frame-indifferent momentum flux. As pointed out by Haller *et al.* (2020), the broadly used linear momentum flux

$$\mathrm{Flux}_{\rho\boldsymbol{v}}(\mathcal{M}(t)) = \int_{\mathcal{M}(t)} \rho\boldsymbol{v}(\boldsymbol{v}\cdot\boldsymbol{n})\,\mathrm{d}A \tag{2.3}$$

is unsuitable for systematic, observer-independent momentum-flux measurements through a material surface $\mathcal{M}(t)$ for several reasons. First, this flux expression originally arises from the application of the Reynold transport theorem to quantify linear momentum carried by fluid trajectories through a non-material control surface. No such trajectory crossings are, however, possible through a material surface. Second, a flux of a quantity through a surface should have the units of that quantity divided by time and multiplied by the surface area, which is not the case for $\mathrm{Flux}_{\rho\boldsymbol{v}}$. Third, $\mathrm{Flux}_{\rho\boldsymbol{v}}$ is not objective because under Euclidean coordinate changes of the form

$$\boldsymbol{x} = \boldsymbol{Q}(t)\boldsymbol{y} + \boldsymbol{b}(t), \quad \boldsymbol{Q}\boldsymbol{Q}^{T} = \boldsymbol{I}, \tag{2.4}$$

the integrand in (2.3) does not transform as an objective velocity field, i.e. we have $\boldsymbol{v}(\boldsymbol{v}\cdot\boldsymbol{n}) \neq \boldsymbol{Q}\tilde{\boldsymbol{v}}(\tilde{\boldsymbol{v}}\cdot\tilde{\boldsymbol{n}})$ for the transformed velocity field

$$\tilde{\boldsymbol{v}} = \boldsymbol{Q}^{T}\left(\boldsymbol{v} - \dot{\boldsymbol{Q}}\boldsymbol{y} - \dot{\boldsymbol{b}}\right). \tag{2.5}$$

This observer dependence is equally true for fluxes obtained from conditionally averaged entrainment velocities used in TNTI studies (e.g. Westerweel *et al.* 2009; Da Silva *et al.* 2014; Eisma *et al.* 2015), as well as projections of momentum flux in the streamwise direction.

To address these shortcomings of $\mathrm{Flux}_{\rho\boldsymbol{v}}$, Haller *et al.* (2020) introduce a frame-indifferent flux for an arbitrary, dynamically active vector field $\boldsymbol{f}(\boldsymbol{x}, t)$ that satisfies a partial differential equation of the form

$$\mathrm{D}\boldsymbol{f}/\mathrm{D}t = \boldsymbol{h}_{\mathrm{vis}} + \boldsymbol{h}_{\text{non-vis}}, \quad \partial_{\boldsymbol{T}_{\mathrm{vis}}}\boldsymbol{h}_{\mathrm{vis}} \neq 0, \quad \partial_{\boldsymbol{T}_{\mathrm{vis}}}\boldsymbol{h}_{\text{non-vis}} = 0. \tag{2.6a–c}$$

Here the term $\boldsymbol{h}_{\mathrm{vis}}(\boldsymbol{x}, t, \boldsymbol{v}, \boldsymbol{f}, \boldsymbol{T}_{\mathrm{vis}})$, arising from diffusive forces (i.e. viscous Cauchy-stresses), is assumed to be an objective vector field, i.e. $\boldsymbol{h}_{\mathrm{vis}} = \boldsymbol{Q}\tilde{\boldsymbol{h}}_{\mathrm{vis}}$. The other term, $\boldsymbol{h}_{\text{non-vis}}(\boldsymbol{x}, t, \boldsymbol{v}, \boldsymbol{f})$, is assumed to have no explicit dependence on viscous forces. Instead, it contains terms originating from the pressure, external forces and possible inertial effects. For instance, if $\boldsymbol{f}$ is the linear momentum of an incompressible Navier–Stokes flow with kinematic viscosity ν, then the Navier–Stokes equations directly imply

$$\boldsymbol{h}_{\mathrm{vis}} = \rho\nu\Delta\boldsymbol{v}, \tag{2.7}$$

which is an objective vector field, because $\Delta\boldsymbol{v} = \boldsymbol{Q}\Delta\tilde{\boldsymbol{v}}$.

The diffusive flux of $\boldsymbol{f}(\boldsymbol{x}, t)$ through $\mathcal{M}(t)$ can then be defined as the surface integral of the diffusive part of the surface-normal material derivative of $\boldsymbol{f}(\boldsymbol{x}, t)$ over $\mathcal{M}(t)$:

$$\Phi\left(\mathcal{M}(t)\right) = \left[\int_{\mathcal{M}(t)} \frac{\mathrm{D}\boldsymbol{f}}{\mathrm{D}t} \cdot \boldsymbol{n}\,\mathrm{d}A\right]_{\mathrm{vis}} = \int_{\mathcal{M}(t)} \boldsymbol{h}_{\mathrm{vis}} \cdot \boldsymbol{n}\,\mathrm{d}A. \tag{2.8}$$

In contrast to (2.3), the diffusive momentum flux $\Phi(\mathcal{M}(t))$ has the correct physical units of momentum flux and is objective. Indeed, under all observer changes of the form (2.4), we obtain $\boldsymbol{h}_{\mathrm{vis}} \cdot \boldsymbol{n}\,\mathrm{d}A = (\boldsymbol{Q}\tilde{\boldsymbol{h}}_{\mathrm{vis}}) \cdot (\boldsymbol{Q}\tilde{\boldsymbol{n}})\,\mathrm{d}\tilde{A} = \tilde{\boldsymbol{h}}_{\mathrm{vis}} \cdot \tilde{\boldsymbol{n}}\,\mathrm{d}\tilde{A}$.

We also define a measure, Φ_N, that is focused solely on quantifying the amount of tangency a surface $\mathcal{M}(t)$ shares with a diffusive momentum flux barrier:

$$\Phi_N\left(\mathcal{M}(t)\right) = \int_{\mathcal{M}(t)} \frac{\boldsymbol{h}_{\mathrm{vis}}}{\|\boldsymbol{h}_{\mathrm{vis}}\|} \cdot \boldsymbol{n}\,\mathrm{d}A. \tag{2.9}$$

In flows with a wide range of $\boldsymbol{h}_{\mathrm{vis}}$ magnitudes, Φ_N provides a normalized measure with no preferential bias towards low-magnitude regions of the flow.

By (2.8), a material surface $\mathcal{M}(t)$ is a perfect instantaneous barrier to diffusive momentum flux if $\boldsymbol{h}_{\mathrm{vis}} \cdot \boldsymbol{n}$ (and thus $\|\boldsymbol{h}_{\mathrm{vis}}\|^{-1}(\boldsymbol{h}_{\mathrm{vis}} \cdot \boldsymbol{n})$) vanishes at each point of $\mathcal{M}(t)$. In other words, the surface $\mathcal{M}(t)$ must be tangent to the vector field $\boldsymbol{h}_{\mathrm{vis}}$ at each of its points, i.e. $\mathcal{M}(t)$ must be an invariant manifold of the differential equation $\boldsymbol{x}' = \boldsymbol{h}_{\mathrm{vis}}$. Here, prime denotes differentiation with respect to the barrier time, s, which parametrizes trajectories of this differential equation.

Specifically, when $\boldsymbol{f}$ is the linear momentum, then we obtain from (2.7) that $\mathcal{M}(t)$ is an invariant manifold of the instantaneous momentum barrier equation

$$\boldsymbol{x}'(s) = \Delta\boldsymbol{v}(\boldsymbol{x}(s), t). \tag{2.10}$$

Here, to speed up trajectory integration, we have dropped the small scalar factor $\rho\nu$ in the definition of $\boldsymbol{h}_{\mathrm{vis}}$ in (2.7). This has no impact on the invariant manifolds (stream surfaces) of $\boldsymbol{h}_{\mathrm{vis}}$.

The barrier time s is a non-dimensional geometric parameter along trajectories of the barrier equations. As such, it has no direct fluid dynamical meaning, much the same way as the geometric parameter τ has no direct physical meaning in the differential equation $\mathrm{d}x/\mathrm{d}\tau = \boldsymbol{v}(\boldsymbol{x}, t)$ defining the instantaneous streamlines of a velocity field. However, if we normalize the barrier vector field to a unit vector at each point, then s will measure precisely the arclength of a computed barrier trajectory. In that case, setting a maximal value s^* for s in our calculations will directly control the barrier length scales revealed by the Lagrangian diagnostics computed on the barrier equations up to the barrier time s^*.

Even at the Reynolds numbers considered here, the diffusive momentum transport is small relative to the total momentum transport, which is dominated by pressure-induced transport. The ratio between diffusive and pressure-induced momentum transport decreases further with increasing Reynolds numbers. We propose, however, that coherent structure boundaries in the flow are distinguished precisely by their ability to inhibit the diffusive component of the momentum transport. Indeed, the transport induced by the pressure gradient also moves coherent structures along with the bulk flow and hence fails to distinguish their boundaries. This view on coherent structure boundaries has been justified analytically for all directionally steady Beltrami solutions of the Navier–Stokes equation, for arbitrary high Reynolds numbers (see Haller *et al.* 2020). The same principle has been verified numerically for diffusive passive scalar transport by Haller, Karrasch & Kogelbauer (2018). They find the observed coherent structures in two-dimensional

geophysical flows coincide with barriers to the diffusive transport of passive scalars (such as the scalar vorticity) for arbitrarily small diffusion.

As a further illustration in Appendix A, we compare perfect barriers to the diffusive momentum transport and perfect barriers to the total momentum transport for an exact Navier–Stokes solution, the time-dependent ABC flow. Due to the dominance of the strongly compressible pressure gradient vector field, the barrier surfaces to total momentum transport accumulate on each other and spiral into fixed points. These characteristically dissipative surfaces are notably dissimilar to the coherent structures seen in tracer experiments and hence would be inconsistent with the view put forward by Westerweel *et al.* (2009) on the relation between barriers of tracer transport and those of momentum transport.

By construction, any 2-D structurally stable invariant manifold $\mathcal{M}(t)$ of the barrier equation (2.10) represents an exact and dynamically robust instantaneous barrier to the diffusive transport of linear momentum. If $\boldsymbol{v}$ is incompressible, then the barrier equation (2.10) is an incompressible, steady dynamical system, given that the time t only plays the role of a parameter (which temporal frame to investigate) and the right-hand side of (2.10) has no explicit dependence on the barrier time s. Therefore, as is well known from chaotic advection studies of 3-D, steady, incompressible flows, structurally stable 2-D invariant manifolds of (2.10) are stable manifolds, unstable manifolds and invariant tori. We note that Haller *et al.* (2020) also extends the barrier equation (2.10) to cover material transport barriers over a finite time interval, but here we will focus on instantaneous momentum barriers. Both the instantaneous and the material barrier equations are objective.

Invariant manifolds (or distinguished stream surfaces) of the barrier equation (2.10) can only be determined numerically and hence will be approximate. We provide two different methods to numerically approximate these barriers with different orders of computational burden. To evaluate the accuracy of our computations and compare the momentum-blocking ability of the computed barriers to nearby features obtained from common vortex and UMZ identification procedures, we will use the surface-area-normalized geometric momentum flux across a surface $\mathcal{M}(t)$,

$$\Psi(\mathcal{M}(t)) = \frac{\int_{\mathcal{M}(t)} |\Delta \boldsymbol{v} \cdot \boldsymbol{n}| \, \mathrm{d}A}{\int_{\mathcal{M}(t)} \mathrm{d}A}. \tag{2.11}$$

This objective quantity does not allow for a cancellation of fluxes in opposite directions and hence vanishes only on perfectly computed momentum barriers. As a result, $\Psi(\mathcal{M}(t))$ provides an objective, non-negative scalar metric for the permeability of the surface $\mathcal{M}(t)$ with respect to momentum transport irrespective of the size of $\mathcal{M}(t)$.

Similarly, the normalized unit barrier field measure,

$$\Psi_N(\mathcal{M}(t)) = \frac{\int_{\mathcal{M}(t)} \left| \dfrac{\Delta \boldsymbol{v}}{\|\Delta \boldsymbol{v}\|} \cdot \boldsymbol{n} \right| \mathrm{d}A}{\int_{\mathcal{M}(t)} \mathrm{d}A}, \tag{2.12}$$

quantifies the degree of tangency between an imperfect barrier and trajectories of the linear momentum barrier field (2.10). This measure provides a clear comparison for surfaces in distinct regions of a flow with different momentum barrier field vector magnitudes by focusing solely on geometry with no bias for small $\Delta \boldsymbol{v}$ values. However, Ψ_N does not have the units of flux and is thus referred to as our barrier field tangency measure.

2.2. *Identification of momentum barrier surfaces*

A number of relevant techniques have been developed in the LCS literature to identify distinguished material surfaces of 3-D steady flows from arrays of trajectories (see Haller 2015, for a review). These methods generally require a numerical differentiation of the flow map or of the velocity field along particle positions. The 3-D steady dynamical system (2.10) already involves two spatial derivatives of the velocity field and further spatial differentiation can only be carried out accurately over sufficiently dense numerical grids (see Haller *et al.* (2020) for examples involving Cauchy–Green strain tensor based diagnostics).

To avoid the numerical issues associated with further spatial differentiation of solutions of (2.10) and to reduce the number of integrated trajectories, here we use very recently developed single-trajectory diagnostics for elliptic (i.e. vortex-type) and hyperbolic LCS, the trajectory rotation average (TRA) and the trajectory stretching exponent (TSE), derived by Haller *et al.* (2021). On any discretized trajectory $\{\boldsymbol{x}(s_i)\}_{i=0}^{N}$ of the barrier equation (2.10) with initial condition $\boldsymbol{x}(s_0)=\boldsymbol{x}(0)=\boldsymbol{x}$, the TRA measures the temporal average of the angular velocity of the trajectory whereas the TSE measures the average hyperbolicity strength along the trajectory. Evaluated in the context of the barrier equation (2.10), these two fields can be computed as

$$\mathrm{TRA}_0^{s_N}(\boldsymbol{x})=\frac{1}{s_N}\sum_{i=0}^{N-1}\cos^{-1}\frac{\langle\dot{\boldsymbol{x}}(s_i),\dot{\boldsymbol{x}}(s_{i+1})\rangle}{|\dot{\boldsymbol{x}}(s_i)|\,|\dot{\boldsymbol{x}}(s_{i+1})|} \tag{2.13}$$

and

$$\mathrm{TSE}_0^{s_N}(\boldsymbol{x})=\frac{1}{s_N}\sum_{i=0}^{N-1}\left|\log\frac{|\dot{\boldsymbol{x}}(s_{i+1})|}{|\dot{\boldsymbol{x}}(s_i)|}\right|. \tag{2.14}$$

To simplify our notation, we have omitted the overbar from the $\mathrm{TRA}_0^{s_N}$ and $\mathrm{TSE}_0^{s_N}$ terms, which was used by Haller *et al.* (2021) to distinguish (2.13) and (2.14) from their versions that allowed for cancellations along trajectories. TRA and TSE computed in (non-objective) physical velocity fields are not objective. In our present context, however, $\mathrm{TRA}_0^{s_N}(\boldsymbol{x})$ and $\mathrm{TSE}_0^{s_N}(\boldsymbol{x})$ are objective fields, because they are computed along trajectories of the objective barrier vector field $\Delta\boldsymbol{v}$.

Calculating trajectories in the unit barrier field

$$\boldsymbol{x}'(s)=\frac{\Delta\boldsymbol{v}(\boldsymbol{x}(s),t)}{|\Delta\boldsymbol{v}(\boldsymbol{x}(s),t)|} \tag{2.15}$$

preserves momentum barrier geometry but standardizes the length of all paths for the same advection time, s_N. TRA and TSE fields calculated from trajectories in the normalized barrier field, NTRA and NTSE, respectively, visualize features in both highly turbulent regions (large $\Delta\boldsymbol{v}$) and less turbulent flow regions, with equal fidelity. As will be shown in the following sections, NTRA and NTSE provide unprecedented comparisons of objective coherent structures over the full range of scales and strengths present in a turbulent flow, and concurrently reveal additional weak structures in less turbulent regions that are not evident from other Eulerian methods.

Haller *et al.* (2021) show that fronts and outer boundaries of nested cylindrical level surfaces of the TRA and TSE fields highlight the same hyperbolic and elliptic invariant manifolds as the finite-time Lyapunov exponent (FTLE, Haller 2015), polar rotation angle (PRA, Farazmand & Haller 2016) and the Lagrangian-averaged vorticity deviation (LAVD, Haller *et al.* 2016), but without relying on the spatial differentiation required by the latter

three diagnostics. The TRA and TSE fields are, therefore, computable from sparse data and their local value is independent of the number and proximity of other trajectories used in the analysis. In upcoming visualizations, influential invariant manifolds of the barrier equation will appear as 2-D surfaces along which TRA or TSE exhibit large changes. The barrier time s_N in (2.13) and (2.14) can be selected arbitrarily, as it is independent of the physical time of the flow data. An increase in s_N enhances details in TRA and TSE visualizations, enabling a gradual, scale-dependent exploration of invariant manifolds in the phase space of the autonomous system (2.10).

For arbitrarily large barrier times, however, the quality of visualization begins to degrade. This is caused by barrier field trajectories leaving neighbourhoods of the finite-sized codimension-one invariant manifolds influencing their initial paths. As TRA and TSE are monotonically non-decreasing functions of s, hyperbolic and elliptic manifolds encountered away from trajectory initial positions will have outsized influence and the diagnostics no longer reflect the features at $\boldsymbol{x}_0$. We thus suggest determining s_N for a given region U as the decorrelation time of instantaneous TRA (or TSE) values. Specifically, for each $\boldsymbol{x}_0 \in U$, we calculate the first zero of the autocorellation

$$\left.\begin{aligned} R(\tau, \boldsymbol{x}_0) &= \sum_{i=0}^{N-1} (f(s_i, \boldsymbol{x}_0) - \bar{f})(f(s_i - \tau, \boldsymbol{x}_0) - \bar{f}), \quad \tau \geq 0, \\ f(s_i, \boldsymbol{x}) &= \mathrm{TRA}_{s_i}^{s_{i+1}}(\boldsymbol{x}_0), \end{aligned}\right\} \tag{2.16}$$

where $\bar{f}$ is the temporal average of f. The median value of this decorrelation time over all $\boldsymbol{x}_0 \in U$ provides a suitable integration time to visualize most invariant manifolds of the barrier field in U with limited interference. We use the same method for determining s_N for the normalized NTRA and NTSE fields in (2.15) as well. We have found that decorrelation times for TRA and TSE to be approximately equal in our numerical studies.

2.3. *Direct numerical simulation data*

To facilitate reproducibility and foster further comparisons with future developments, we have selected from the publicly available Johns Hopkins University Turbulence Database (JHTDB) a direct numerical simulation of a $Re_\tau = 1000$ channel flow (Perlman *et al.* 2007; Li *et al.* 2008; Graham *et al.* 2016). On this data set, we compare UMZ interfaces and velocity-gradient-based vortices with perfect instantaneous barriers to the diffusive transport of linear momentum. While UMZ studies are typically performed on turbulent boundary layers, Kwon *et al.* (2014) and Fan *et al.* (2019) have argued for the generalization of such features to channel flows as well.

The JHTDB channel flow data are available on a $2048 \times 512 \times 1536$ grid for a domain of size $8\pi h \times 2h \times 3\pi h$, where h is the half-channel height. The DNS timestep $\Delta t = 0.0013$ in non-dimensional simulation units, with the stored simulation time step, $\delta t = 5\Delta t$, or approximately one channel flow-through time. The analysis herein is conducted over 100 frames spanning the entire simulation database with a duration of 4000 channel flow-through times from $t = 0$ to $t = 26$. All figures and analysis will be displayed in non-dimensional half-channel height units ($h = 1$). This dataset has been used in a number of studies, most notably by Bautista *et al.* (2019) to evaluate a model of velocity-based uniform momentum zones, and by Jie, Andersson & Zhao (2021) to investigate inertial particle collection in the quiescent core.

To account for the instability caused by numerical integration through large $\Delta \boldsymbol{v}$ fluctuations near the channel walls, we have implemented a quadratic buffer in the lower

viscous sublayer, within five viscous lengths or $0.005h$ from the wall. That is, for $0.995h \leq |y| \leq 1$, we define $\Delta \boldsymbol{v}(x, y) = \boldsymbol{v}(x, \pm 0.995h)((y \mp 1)/(0.995h \mp 1))^2$ for the appropriate wall. Eyink, Gupta & Zaki (2020) examined this region and calculated these heights to be well within the viscous sublayer for our JHU channel. We find that this minimal buffer zone does not modify the visualization of structure in the momentum barrier field, but it significantly expedites calculations and aids in fixed time step advection of trajectories at the long time scales necessary for determining optimal decorrelation times in (2.16).

2.4. *Computational consideration*

Common to Lagrangian-trajectory diagnostics, the computational burden of calculating TRA and TSE in the vector fields (2.10) and (2.15) primarily comes from the accurate integration of trajectories which requires interpolating large vector fields to determine trajectory velocities. The present analysis was conducted in MATLAB on either a professional workstation for specific examples, or a high performance computing cluster to calculate large numbers of TRA and TSE fields in large domains. Using a fourth-order Runge–Kutte integration scheme with 10 000 time steps on a 2.3 GHz, 18 Core, 128 GB iMac Pro, TRA and TSE values from 10 000 initial positions, $\boldsymbol{x}_0$, can be computed in an interpolated vector field of $100 \times 100 \times 100$ grid points, with spatial dimensions $1.2h \times 0.6h \times 0.6h$, in a wall-clock time of 5 s. This can clearly be improved upon in more computationally efficient programming languages.

As one increases the spatial dimensions of initial conditions $\boldsymbol{x}_0$, the flow domain used in the interpolation needs to be increased to avoid boundary effects, as in Eisma *et al.* (2021). This, in turn, decreases the speed of the computations. We thus calculate the TRA and TSE fields in (2.10) using a patchwork of initial positions in flow domains with large margins so as to avoid trajectories leaving the domain. In the subsequent analysis, we found exemplary visualization is possible with spatial resolutions of the order of 1 to 10 viscous lengths ($10^{-3}h$ to $10^{-2}h$), with the finer resolutions beneficial for smooth flux-minimizing isosurface extraction. Parallelized MATLAB scripts to calculate TRA and TSE are available on github (https://github.com/haller-group/TRA_TSE).

3. Results

3.1. *Objective momentum transport barrier visualization*

Figure 2 compares a common turbulence visualization diagnostics, the vorticity magnitude, with the NTRA field computed for the normalized momentum barrier equation (2.15) on a streamwise-wall-normal plane of initial conditions in the channel at the non-dimensional DNS time $t = 0.065 = 5\delta t$. The predominant channel flow is in the positive x-direction with channel walls at $y = \pm 1$. Both diagnostic fields in figure 2 were generated from precisely the same velocity field, and were calculated and visualized at the same spatial resolution ($\delta_x = \delta_y = 10^{-3}$). The vorticity picture is indicative of the scale and resolution of structures that are captured by velocity and velocity-gradient-based level-set methods. The barrier trajectories $\boldsymbol{x}(s)$ used in these simulations were advected under the 3-D normalized barrier equation until $s_N = 0.5$, the order of decorrelation time for the entire channel.

The shear generated by the upper and lower channel walls is evident from the high rates of trajectory rotation and vorticity. Surprisingly, in the NTRA field, there is strong evidence of many more vortical momentum barriers in the centre of the channel, which is typically viewed as a quiescent region. This shows that while there are still many complex vortex interactions occurring in the region, their relatively weaker signature makes them

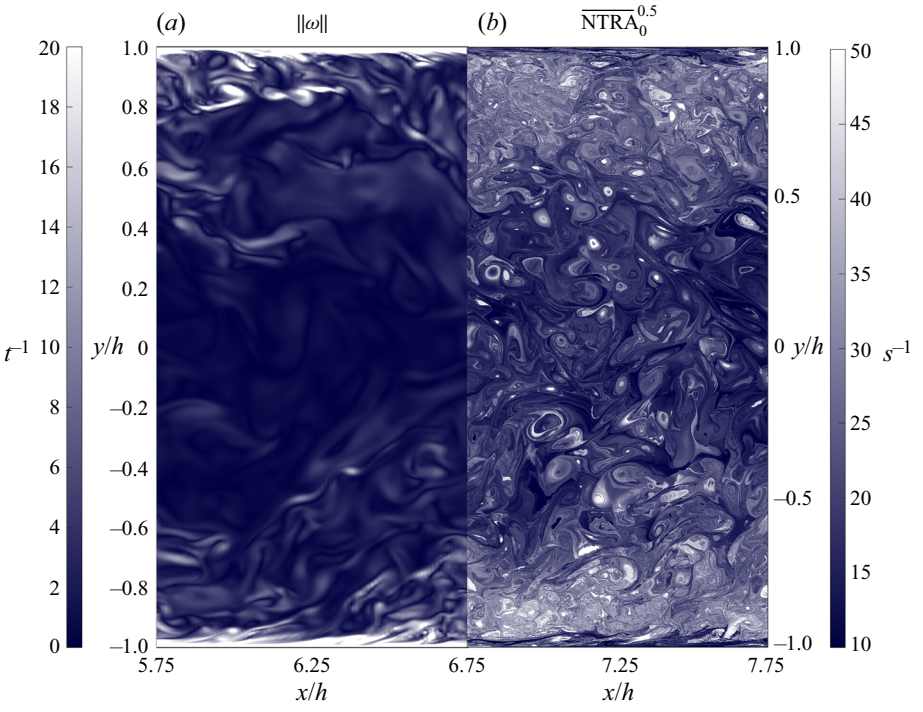

Figure 2. A streamwise-wall-normal plane of the $Re_\tau = 1000$ JHTDB Channel Flow coloured by vorticity magnitude (*a*) and $\overline{\mathrm{NTRA}}_0^{0.5}$ (*b*). Both visualizations of turbulent features are calculated at the same spatial resolution from the same velocity data at one time step. The enhanced visualization possible with $\overline{\mathrm{NTRA}}$ provides a striking comparison with classic techniques and illuminates faint and weak structure in the centre of the channel while maintaining objectivity.

impossible to identify in the weak gradients and uniformly low vorticity values. Thus, the NTRA field provides an enhanced visualization of structures at a much wider range of spatial scales and structure strengths for the same underlying velocity data. For identifying boundaries and the structure extraction discussed in the next sections, we find the large changes evident in TRA and TSE fields to be most beneficial. At the same time, NTRA and NTSE continue to provide homogeneous fidelity visualizations of barriers in large domains that contain a wide range of vector magnitudes.

Zooming in on the turbulent wall-region, we find the degree of detail of TRA fields for the original barrier equations (2.10) is also unattainable by classic velocity-gradient based vortex diagnostics. This first-order benefit can be seen in figure 3, in which TRA is compared with Q, λ_2 and λ_{ci} (swirling strength) (Hunt *et al.* 1988; Jeong & Hussain 1995; Zhou *et al.* 1999) for a streamwise-wall-normal (x, y) plane adjacent to the lower channel wall. Again, all four plots were generated with the same spatial resolution from the same single velocity snapshot of the DNS data. In contrast to the other plots, the TRA is objective and reveals substantially more of the complexity of the flow for the decorrelation advection time $s_N = 10^{-4}$.

The TRA plot in figure 3 reveals a complex connection network and a layering of unique rotational features not present in the velocity-gradient-based diagnostics. All colourmaps have been chosen to reveal the full range of metric values, though gradient-based approaches suffer from the same issues as in figure 2. The level of detail in the TRA

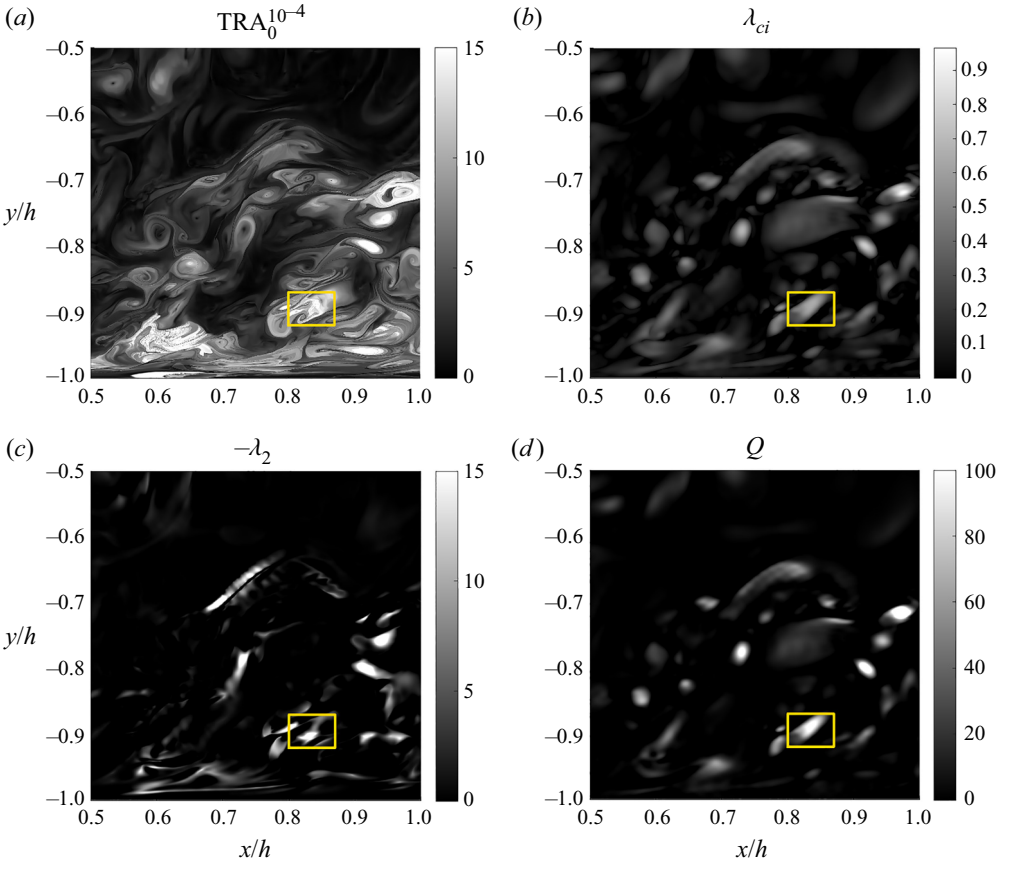

Figure 3. Comparison of the objective TRA field with non-objective, velocity-gradient-based vortex identification diagnostics in the highly turbulent region at the channel wall. Panels (*a–d*) are computed with the same spatial resolution from the same single velocity snapshot of the DNS data.

field provides increased accuracy in vortex detection. For example, at approximately $(x/h, y/h) = (0.8, -0.9)$, there is a clear maximum in all three velocity-gradient-based metrics, which suggests the potential presence of a coherent vortex (yellow box). Upon closer inspection of the TRA in the same region, however, we find a lack of nested cylindrical TRA level surfaces. Instead, filamenting invariant surfaces of the barrier equation are present that are not structurally stable and hence do not define vortical barriers to momentum transport. The TRA field discerns these important structural features and has a significant advantage in preventing false-positive vortex identifications. Furthermore, these details are useful for accurately tracking individual features from one time to the next, as will be discussed in § 3.4. An internal layering close to the wall is also present in the TRA field, as is the organization of vortices around a clearer transition between the more turbulent wall region and the less turbulent channel core. We discuss this interface in more detail in § 3.3.

3.2. *Momentum-trapping vortices*

In 2-D cross-sections of the flow, vortex boundaries can be located as the outermost members of nested families of closed level curves of the TRA. Launching trajectories

of the 3-D barrier equation (2.10) from these boundary curves generates instantaneous, vortical momentum barrier surfaces in the full 3-D flow. In direct contrast to velocity-gradient-based vortex identification practices, this process is devoid of any user-defined parameters beyond a choice of spatial resolution of barrier-field trajectory initial positions, which only serves to control the level of detail in the TRA field. In contrast to velocity and velocity-gradient-based diagnostics, increasing the spatial resolution of TRA and TSE fields beyond that of the underlying velocity field can continue to increase the structural information revealed because of the dummy time barrier field integration.

Figure 4 shows one example of our momentum-trapping vortex identification method, with barrier trajectories starting from the $z = 2.55h$ plane. Figure 4(a) also reveals a strong similarity between the detailed structures in the TRA field and the material boundary layer structures visualized in smoke experiments (figure 1), to be discussed in more detail in § 3.4. Through a simple search algorithm on TRA contours, we have identified a region with a nested set of closed TRA level curves. By extracting all TRA contours that span the range of values present, we can isolate the closed and convex contours. The outermost convex boundary curve for each vortex obtained in this fashion is highlighted in figure 4(b). Using these vortex boundaries as initial positions, we can advect a dense set of trajectories in the barrier field in forward and backward barrier time to obtain the exact momentum transport barriers seen in figure 4(c). If choosing smaller members of the set of closed level curves of the TRA as a curve of initial conditions, we obtain an internal foliation of the vortex by smaller cylindrical momentum barriers. These block radial diffusive momentum transport within the vortex. The details of this process are described in Algorithm 1.

A simpler but only approximate way to visualize objective momentum barriers is to plot level surfaces of the TRA field. This is inspired by the observation that structurally stable elliptic invariant manifolds (such as invariant tori) of the barrier equation (2.10) will be spanned by trajectories with the same averaged angular velocities in the limit of $s_N \to \infty$. For finite values of s_N, this relationship is only approximate and hence TRA isosurfaces are only proxies to exact invariant manifolds formed by the trajectories of (2.10). For such finite values, nearby particle trajectories that do not lie on the same invariant manifold may also accumulate the same TRA value. As a consequence, contour-plotting algorithms may connect approximations of different momentum barriers into one approximate level surface. Such artefacts arising from this simplified visualization can be discounted by launching actual barrier trajectories of (2.10) from the intersections of TRA level sets from a reference cross-section and discounting parts of the level surface whose distance from such barrier trajectories exceeds a tolerance value.

An example of this isosurface separation process is detailed in figure 5. Starting with the vortex identified by the blue 2-D convex contour in figure 4, multiple concentric 3-D TRA shells can be seen in figure 5. The outer and inner blue shells correspond with $\mathrm{TRA}_0^{10^{-3}} = 11$ level sets, and the two red shells correspond to a higher rotation rate, the $\mathrm{TRA}_0^{10^{-3}} = 16$ level set. Probability distribution functions of the distance between each isosurface and the barrier field streamlines generated from their intersection with the $z = 2.55h$ plane are shown inset in figure 5. As is typical for all vortices we have investigated, there is a clear p.d.f. peak close to zero that can be automatically isolated for both isosurfaces with a variety of algorithms, including inflection points or kernel density estimation. These values correspond with points on the TRA level surface that closely approximate the momentum-blocking invariant manifolds in figure 4. Once points with streamsurface-distances outside this peak are removed from the visualization, the separation between each vortex shell is clearly visible. The selected distances of separation

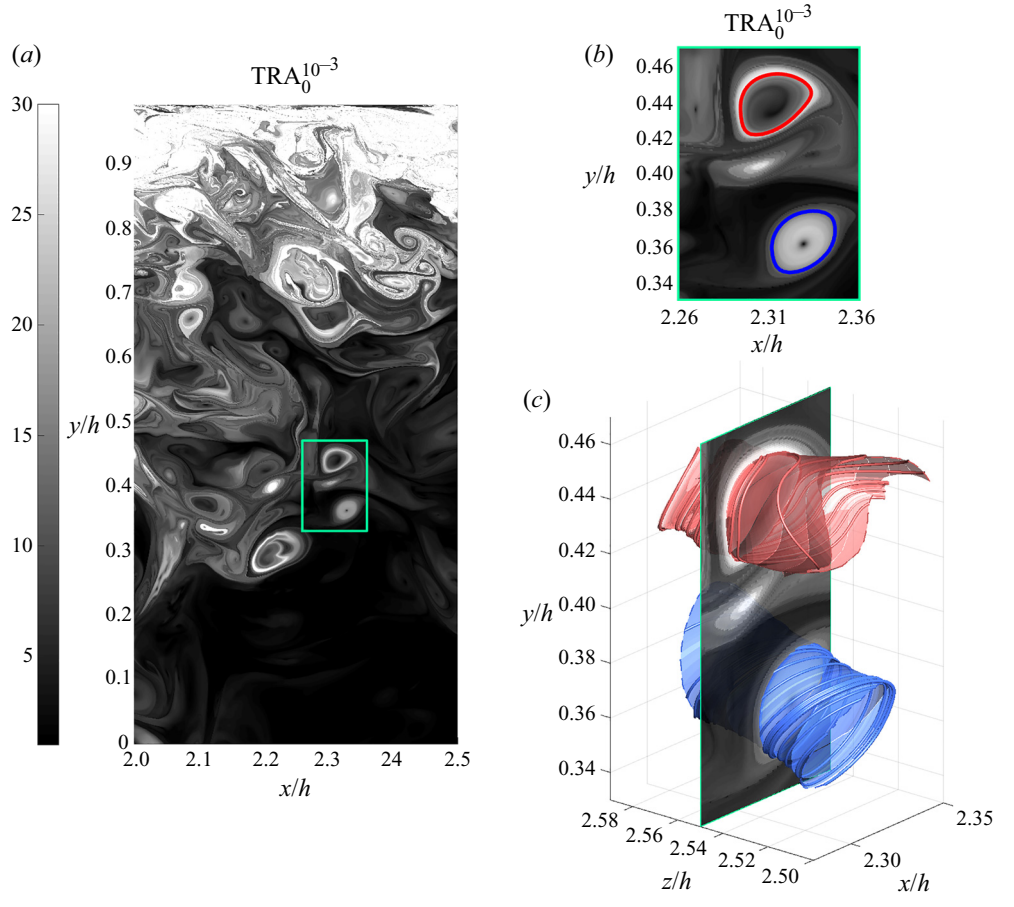

Figure 4. Momentum-trapping vortices in the turbulent channel flow. The vortex boundaries are determined as streamsurfaces of $\Delta \boldsymbol{v}$ that intersect the plane of investigation ($z = 2.55$) along outermost closed and convex TRA contours.

used in this visualization are shown in the inset p.d.f.s as dashed vertical lines. The details of this process are also summarized in Algorithm 1.

To quantify how well outermost cylindrical TRA level surfaces, denoted $\mathcal{I}_{TRA}$, approximate true momentum barriers, we calculate the normalized objective geometric flux $\Psi(\mathcal{I}_{TRA})$ defined in (2.11), which vanishes only on perfect barriers to momentum transport. For comparison, we also extract representative isosurfaces of λ_{ci}, λ_2 and Q, denoted by $\mathcal{I}_{\lambda_{ci}}$, $\mathcal{I}_{\lambda_2}$ and $\mathcal{I}_Q$, in the same 3-D fluid volume and calculate Ψ on these surfaces as well. While there are various empirical values proposed for representative $\mathcal{I}_{\lambda_{ci}}$, $\mathcal{I}_{\lambda_2}$ and $\mathcal{I}_Q$ isosurfaces (see, e.g. Jeong & Hussain 1995; Zhou *et al.* 1999; Ganapathisubramani, Longmire & Marusic 2006; Gao *et al.* 2011; Dong & Tian 2020), we initially generate surfaces that correspond with their originally argued value, dividing strain-dominated and rotation-dominated regions. This value is zero for all velocity-gradient-based metrics (see Hunt *et al.* 1988; Jeong & Hussain 1995; Zhou *et al.* 1999).

The isosurfaces generated for each scalar metric are displayed in figure 6. As common practice, the swirling strength λ_{ci} has been normalized by its maximum value in the volume of interest. Each isosurface is shown as it intersects the $z = 2.55h$ plane coloured by

Algorithm 1 Extracting momentum vortex cores

1. For a co-dimension 0 domain of interest $U \subset \mathbb{R}^3$, select a grid of initial conditions $\boldsymbol{x}_0 \in U$.
2. Choose an initial barrier time estimate ϵ and calculate the discretized trajectories $\{\boldsymbol{x}(s_i)\}_{i=0}^{N}$ in the barrier field (2.10) where $\epsilon = s_N$.
3. For each trajectory $\boldsymbol{x}(s_i)_{i=0}^{N}$, calculate $f(s_i, \boldsymbol{x})$ following (2.16) and (2.13).
4. Determine the optimal barrier time ϵ_0 as the first-zero crossing of the autocorrelation of f as defined in (2.16). If no zero-crossing exists, repeat Steps 2–4 with progressively larger ϵ until a zero-crossing exists.
5. Repeat Steps 1–2 for $\epsilon_0 = s_N$ and calculate $\mathrm{TRA}_0^{s_N}$ following (2.13).
6. Select a plane of interest of initial conditions that intersects U and extract iso-contours in that plane for the range of TRA values generated in Step 5. Record only the outermost closed convex contours $\{\gamma_j\}$ as vortex core candidates.

7a **To extract the invariant manifold** of (2.10) that intersects a given curve γ_j, identify trajectories $\{\boldsymbol{x}_{\gamma_j}(s_i)\}_{i=0}^{N}$ such that $\boldsymbol{x}_{\gamma_j}(0) \in \gamma_j$. If an insufficient number of trajectories exist, identify points in γ_j through interpolation to obtain a set $\boldsymbol{x}_{\gamma_j}(0)$ and repeat Step 2 with $s_N = \epsilon_0$.

7b Given a sufficiently dense set of trajectories, the co-dimension 1 vortex core be identified by linear interpolation between nearest points in the set of trajectory data $\{\boldsymbol{x}_{\gamma_j}(s_i)\}_{i=0}^{N} \in \mathbb{R}^3$.

8a **To obtain a level-surface approximation** of a momentum vortex core that intersects a given closed contour γ_j, extract that TRA isosurface $\mathcal{I}_{TRA}$ that intersects γ_j.

8b Repeat Step 7a and calculate the distance between points in $\mathcal{I}_{TRA}$ and nearest points in $\{\boldsymbol{x}_{\gamma_j}(s_i)\}_{i=0}^{N}$.

8c Calculate the p.d.f. of these distances. Here, $\mathcal{I}_{TRA}$ will be sufficiently close to $\{\boldsymbol{x}_{\gamma_j}(s_i)\}_{i=0}^{N}$ for many points, resulting in a distinct peak in the probability density function (p.d.f.) near zero. Refine $\mathcal{I}_{TRA}$ to only include points in this near-zero peak.

9. Steps 5–8 can be repeated for $-\epsilon_0$ to further expand the extracted vortex core.

$\mathrm{TRA}_0^{10^{-3}}$. For the three velocity-gradient-based diagnostics, the corresponding diagnostic field on $z = 2.55h$ is shown inset next to the volumes. The surface-area-normalized momentum flux across each isosurface is also noted to the right of each respective volume.

In the $z = 2.55h$ insets, λ_{ci}, λ_2 and Q values all show some indication of the presence of the upper vortex from the TRA field, though evidence of the lower vortex is not present in λ_2. This suggest the presence of our physical momentum barriers may have influenced these scalar fields, but the metrics are ineffective at predicting where the transport barriers lie. Even as simplified approximations of true linear-momentum barriers, TRA isosurfaces are still quite effective momentum transport barriers. Indeed, $\Psi(\mathcal{I}_{TRA})$ is only 24 % of $\Psi(\mathcal{I}_{\lambda_{ci}})$, 22 % of $\Psi(\mathcal{I}_{\lambda_2})$ and 26 % of $\Psi(\mathcal{I}_Q)$. Recall that $\Psi = 0$ for the invariant manifolds in figure 4 that $\mathcal{I}_{TRA}$ is approximating here.

We have found that with increased numerical accuracy in our barrier field integrations, TRA calculations improved and resulted in a further decrease in $\Psi(\mathcal{I}_{TRA})$. This indicates one can more closely approximate the true momentum transport barriers with more computational expense when a particular region of interest is identified. We have not

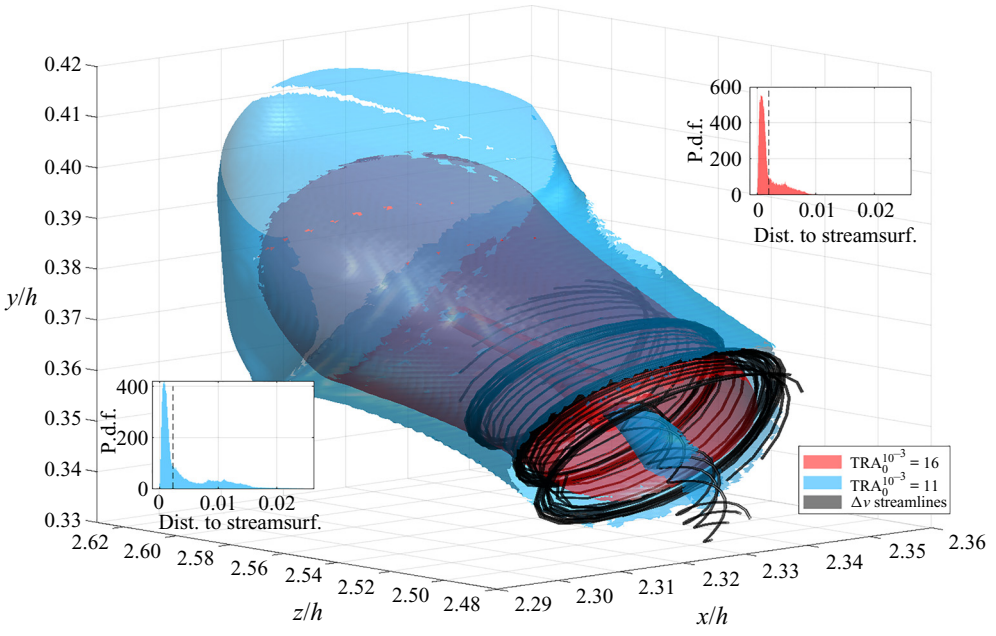

Figure 5. TRA isosurfaces as approximations to the momentum transport barriers shown in figure 4. Blue and red surfaces correspond with two distinct $\mathrm{TRA}_0^{10^{-3}}$ values. Shown in black are a subset of streamlines initiated on the $\mathrm{TRA}_0^{10^{-3}} = 16$ contour on the $z = 2.55$ plane. Inset are probability distribution functions of the minimum distance of unfiltered surface points to streamlines initialized on TRA contours at $z = 2.55$.

found analogous numerical improvements in flux reduction upon refining the spatial differentiation or resolution of the velocity-gradient-based methods. Overall, we find that the classic vortex diagnostics we have tested do not provide a clear indication of a pair of 3-D vortices when one directly implements the criteria arising from their theoretical derivations. Rather, one must hand pick values to obtain a vortical feature in two or three dimensions as noted by Dong & Tian (2020) and Dubief & Delcayre (2000). This is problematic in turbulent flows where there is no ground-truth of structure topology against which one can validate their hypothesized threshold values.

To accommodate the wide range of empirical or heuristic thresholds used in the literature, we have also performed the same flux calculations for λ_{ci}, λ_2 and Q-isosurfaces for a range of values that includes and exceeds available suggestions found in the literature. The resulting fluxes are displayed in figure 7. Note that $\mathcal{I}_{TRA}$ in blue continues to outperform all other diagnostics over the whole range of empirical threshold values for the latter diagnostics.

In figure 8, we verify the surface tangency of arbitrary-valued TRA level-surfaces with invariant manifolds. If isosurfaces of a given scalar field were exact streamsurfaces of the barrier equation, then their normals (i.e. the gradient of that scalar field) would be perpendicular to $\Delta \boldsymbol{v}$. Each subplot of figure 8 shows the probability distribution of inner products of normalized scalar field gradient vectors with the normalized barrier field, $\Delta \boldsymbol{v}/|\Delta \boldsymbol{v}|$, over the entire 3-D volume containing our vortices ($[2.26, 2.36] \times [0.34, 0.37] \times [2.5, 2.6]$). These are precisely distributions of the signed integrands of the numerator in (2.12). Vertical dashed lines mark a $\pm 5^\circ$ deviation from perfect agreement between momentum barriers and barriers generated by each diagnostic level set. Notably, there is a clear peak around 0 for $\nabla \mathrm{TRA}_0^{10^{-3}}$, while a nearly uniform (random) distribution

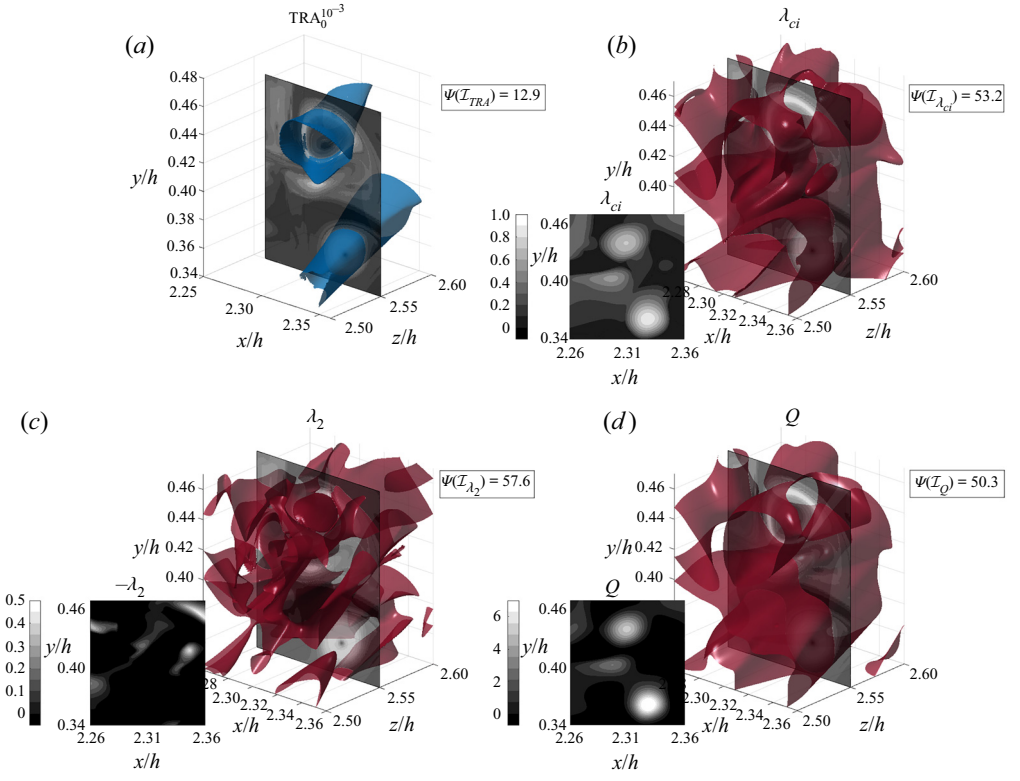

Figure 6. Comparison of area-normalized objective momentum flux values for vortex boundaries identified from different vortex identification methods.

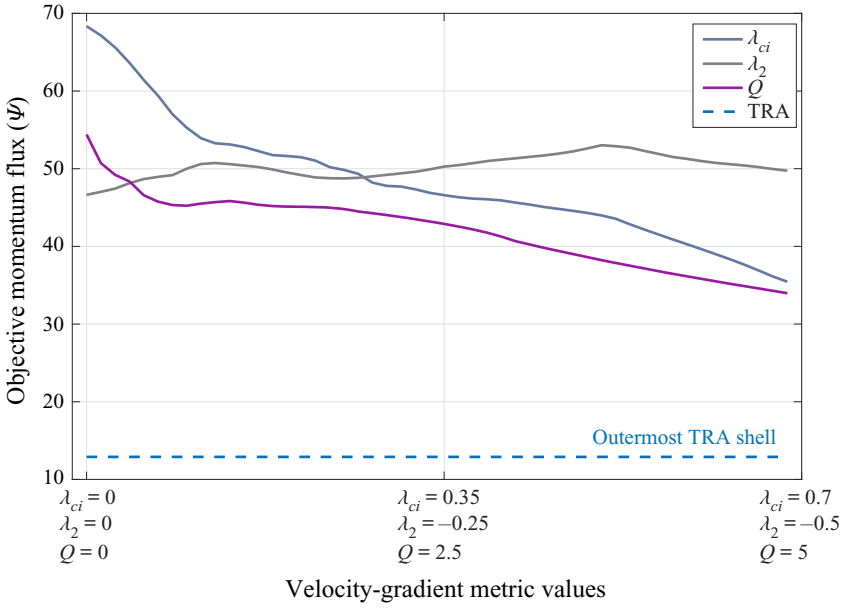

Figure 7. Comparison of momentum flux through $\mathcal{I}_{TRA}$ and through structure boundaries defined by a wide range of isosurface values for the λ_{ci}, λ_2 and Q metrics.

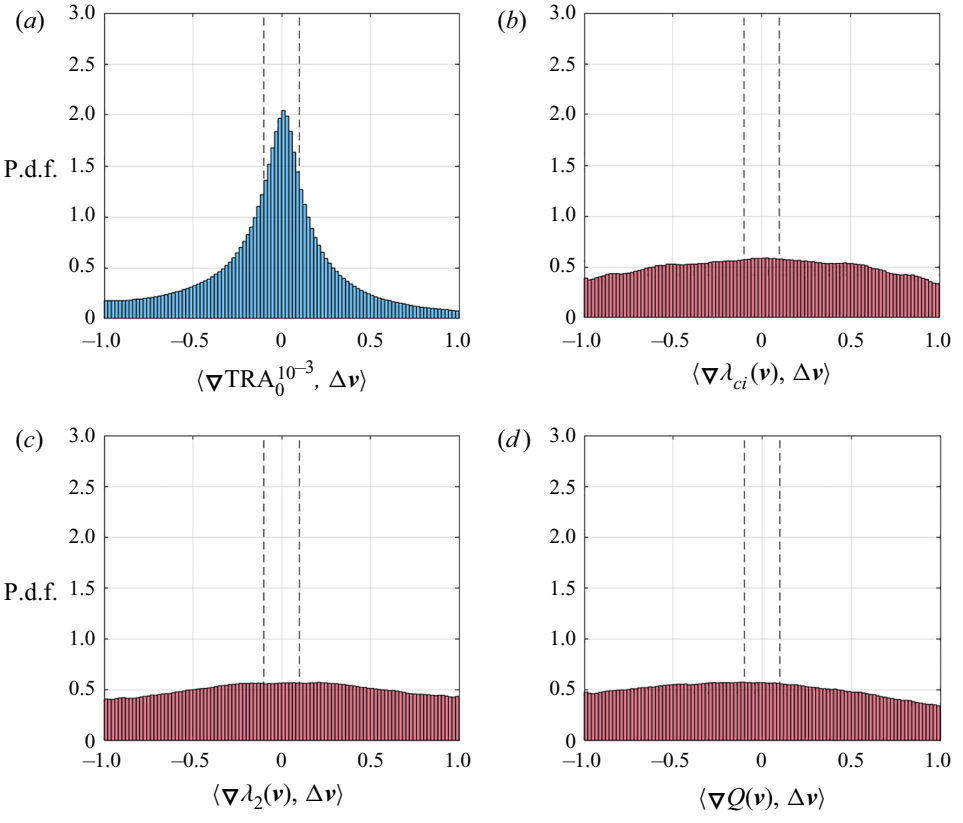

Figure 8. Probability distributions of the normalized inner product of momentum barrier field vectors and isosurface normals for TRA and the three standard velocity-gradient-based diagnostics for a 3-D rectangular volume of fluid containing the vortices in figure 6. The clear singular peak around 0 in the TRA p.d.f. indicates a strong agreement between TRA surfaces and the underlying momentum transport blocking interfaces for both elliptic and hyperbolic surfaces. Similar behaviour does not exist for the other three diagnostics. A $\pm 5^\circ$ difference between surface tangents and barrier vectors is delimited by dashed lines.

can be seen for angles between barrier field vectors and velocity-gradient-based isosurface normals.

As the linear-momentum barrier vector field $\Delta \boldsymbol{v}$ is objective, extracting the classic λ_{ci}, λ_2 and Q level surfaces from the $\Delta \boldsymbol{v}$ field would also be an objective procedure, unlike extracting these level surfaces from the velocity field $\boldsymbol{v}$, as originally intended for these diagnostics. To see if such an objectivization would benefit these criteria, we have carried out the same statistical structure-tangency analysis with the λ_{ci}, λ_2 and Q metrics now applied to the barrier field $\Delta \boldsymbol{v}$. While the resulting p.d.f.s in figure 9 now show a moderate rise near zero for each classic vortex diagnostic, TRA level-sets still outperform the other diagnostics in their ability to block the viscous transport of momentum. This suggests that TRA level sets are overall close approximations to the perfect momentum barriers formed by invariant manifolds of the barrier equation (2.10).

3.3. *Momentum transport barrier interfaces*

We have, so far, used level surfaces of the TRA field for the approximate visualization of vortices with a perfect instantaneous momentum-trapping property. We can also use

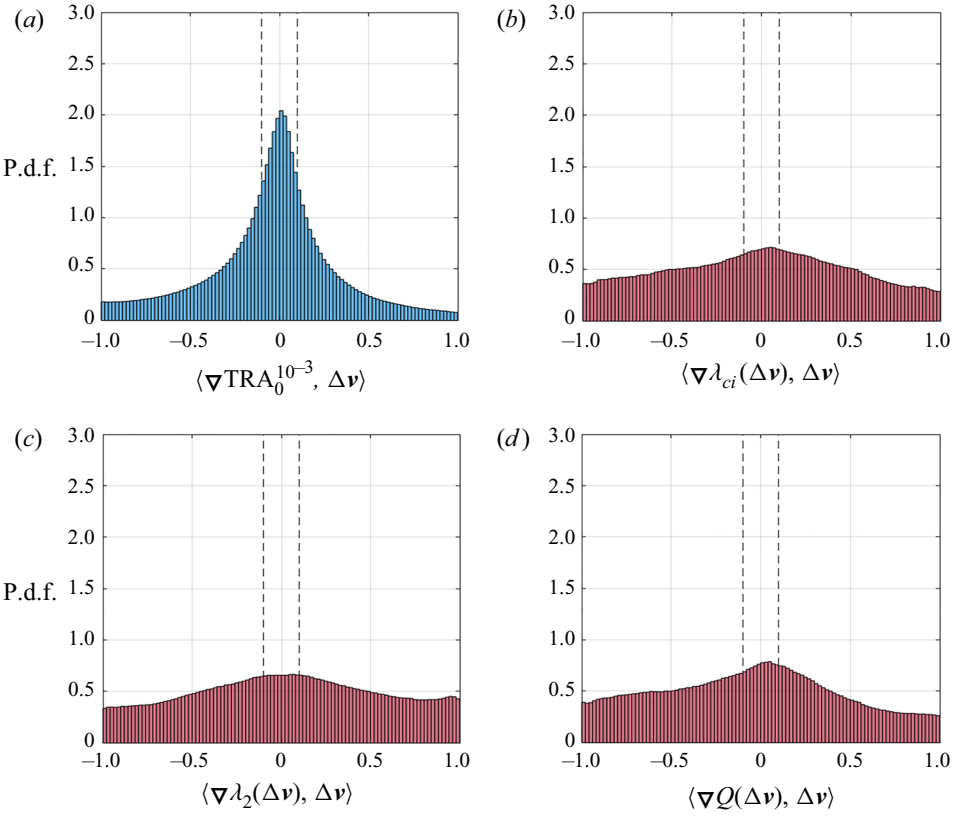

Figure 9. Same as figure 8, but with the λ_{ci}, λ_2 and Q metrics computed for the barrier equation (2.10).

the TSE field to interrogate the momentum barrier equation more globally to locate momentum-blocking interfaces between more and less turbulent areas of the flow. This can be achieved by constructing streamsurfaces of the barrier equation that partition the flow into wall-parallel domains with boundaries that span the channel in the wall-parallel directions. We use TSE fields to aid in this interface identification as their level surfaces separate regions of distinct degrees of stretching in a manner analogous to hyperbolic invariant manifolds. We use the single smoothest interface as this provides the barrier with the least folding. As shown in figure 10, there are multiple spanning TSE interfaces in a given domain. These interfaces contour around vortices that compose large scale motions. After analysing 100 temporal frames of TSE fields, we find that using the average straightest contours allows us to connect the outermost contour around these vortices. This selection can be modified for other flow-specific criteria, and a statistical analysis of all candidate TSE interfaces is conducted in § 3.4.

We now describe a simple, automated algorithm for identifying such objective MTB as a physics-based alternative to the currently used TNTI or UMZ interface identification processes (Adrian *et al.* 2000*b*; Da Silva *et al.* 2014; De Silva *et al.* 2015). This algorithm is also sketched in Algorithm 2. As with our vortex identification, when using the trajectory decorrelation time for TSE calculations, we only use one free parameter in our MTB algorithm: the choice of spatial resolution, which is approximately one viscous length in all directions. This ultimately controls the level of detail in the MTB interfaces and their momentum-blocking ability. In contrast to common TNTI or UMZ level-surface

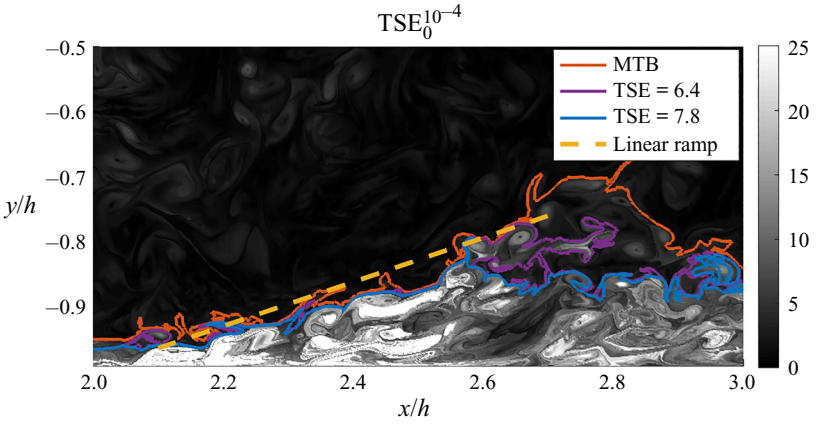

Figure 10. TSE contours with the smoothest contour selected as an MTB. A linear ramp identified by a linear-fitting search is also drawn. Note that the MTB is more effective at contouring around the outside of vortices whereas the other two TSE contours filament and penetrate the interiors of vortices.

approaches, we can progressively improve our momentum-barrier identifications by calculating TSE at progressively finer resolutions beyond the underlying velocity grid. This improves surface triangulations and enhances tangency with invariant manifolds in the barrier field (2.10).

Algorithm 2 Extracting MTB

1. For a co-dimension 0 domain of interest $U \subset \mathbb{R}^3$, select a grid of initial conditions $\boldsymbol{x}_0 \in U$.
2. Determine the optimal barrier time ϵ_0 using TSE calculations (instead of TRA) in Steps 2–4 in the vortex core extraction algorithm.
3. For each streamwise-wall-normal hyperplane V_z that intersects U, extract iso-contours in V_z for the range of TSE values present in V_z. Record only the contours $\{\gamma_j\}$ that span the full streamwise width of the domain.
4. Refine $\{\gamma_j\}$ to corresponding TSE values with contours that span the domain for every V_z.
5. Select the TSE value such that the corresponding γ_j span each V_z with minimal length.
6. Extract the connected TSE isosurface corresponding to this TSE value that intersects the γ_j of interest.

We begin this algorithm by calculating the TSE for the active barrier equation (2.10) on a 3-D domain of interest. Here we use the decorrelation time as determined for the wall-proximal (outer) quarter of the channel ($|y| \geq 0.75$) in an effort to visualize the most turbulent and complex momentum blocking structures ($s_N = 10^{-4}$) emanating from the wall. Through a sensitivity analysis, we found MTB identification to be consistent over six orders of magnitude of s_N, but the visual clarity of near-wall structures begins to deteriorate away from our chosen s_N. Note that these six orders of magnitude relate to the integration time of a trajectory in the barrier field equations, and not to a physical spatial or temporal dimension. For example, a longer integration time may allow initially adjacent particles to separate to a larger degree, or for a trajectory in a vortex core to

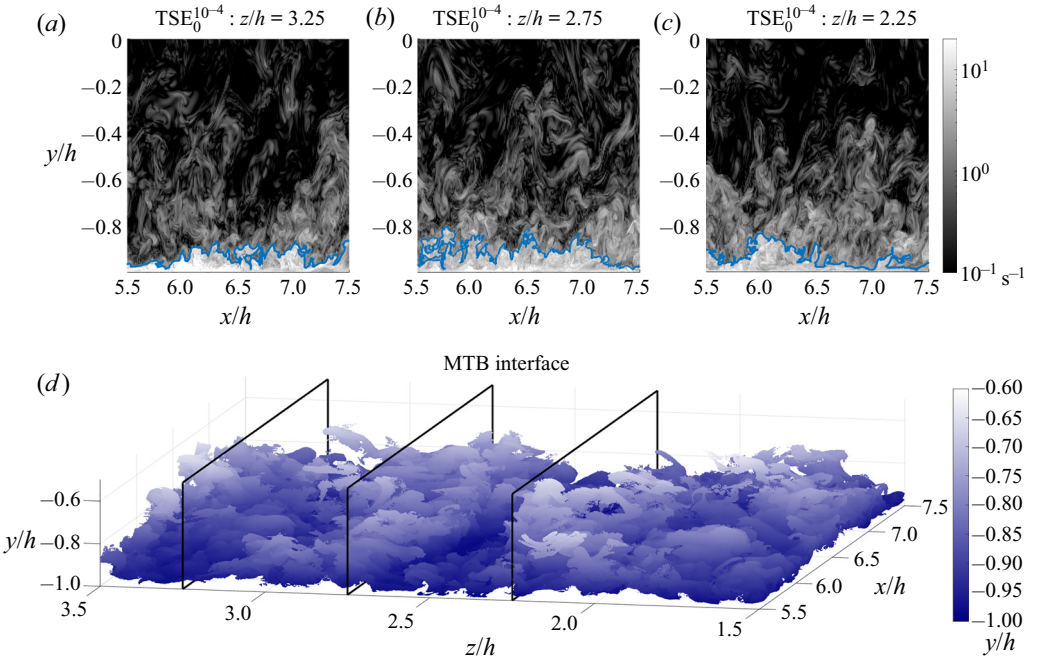

Figure 11. (*a–c*) Process of selecting the TSE contour that spans a domain of interest most efficiently among many adjacent 2-D slices. (*d*) Corresponding TSE-derived momentum transport barrier (MTB) coloured by *y*-values.

circulate more, thus allowing for more distinct TSE and TRA contours, but not necessarily a different size of spatial features. As well, the $s_N = 0$ limit exists, providing an estimate of the structures detailed here. The decorrelation time for visualization close to the wall is shorter than the value $s_N = 10^{-3}$ calculated for our focus on vortices near the centre of the channel as the magnitude of the $\Delta \boldsymbol{v}$ is much greater near the wall and a shorter integration time is sufficient to obtain the same degree of detail.

To reduce the computational burden of finding the smoothest domain-spanning interface, we first perform a series of 2-D approximations. We select a set of $n \geq 1$ streamwise-wall-normal planes and identify the shortest TSE contour in each plane that divides the plane into a lower (wall-adjacent) and upper (central) region. For example, see the candidate spanning contours at TSE = 3.11 for multiple z planes in figure 11(*a–c*). Each such shortest, in-plane contour has a corresponding TSE value whose corresponding 2-D TSE level surface is a candidate for an MTB interface. Of these candidate surfaces, we finally select the 2-D TSE level surface whose intersection curves with the n streamwise-wall-normal planes have the lowest maximum length. This procedure, therefore, yields the MTB interface as the TSE level surface that divides the flow roughly into parallel near-wall and mean-flow regions while maintaining as low a curvature as possible. The corresponding lower half-channel MTB determined from this algorithm can be see in figure 11(*d*). The boundaries of the three upper planes of contour investigation are drawn in black. More involved algorithms targeting the same objective can certainly be devised but will likely come with increased computational cost.

The MTB interface in figure 11 is a complex structure that reveals connections of multiple vortices as they collect and migrate from the channel wall to the less turbulent centre of the channel. The MTB has been shaded by the distance from the lower

channel wall to help illuminate heterogeneity in the wall-normal extent of this MTB. Qualitatively familiar material features from smoke and dye experiments can be seen in this objective barrier. The organization of characteristic interface eddies documented by Falco (1977) and Head & Bandyopadhyay (1981) are evident along the MTB as well as the large-scale streamwise streaky structures of Kline *et al.* (1967), with a spanwise spacing of approximately $0.75h$. There is also a striking similarity to scalar concentrations visualized in jet-driven TNTI (e.g. Westerweel *et al.* 2009).

The MTB interface obtained in this fashion approximates the flattest invariant manifold of the barrier equation that divides the flow into two disjoint quasi-wall-parallel layers with minimal diffusive momentum transport between them. The low-curvature requirement in the construction of this interface forces it to avoid highly turbulent regions and effectively connect outer regions of the momentum-trapping vortices that we have already discussed.

To illustrate this behaviour, in figure 12, we focus on a small subdomain of figure 11 and compare our interface with two commonly used UMZ and TNTI identification diagnostics, vorticity and normalized streamwise velocity. While high-shear regions have been associated with UMZ interfaces (Hunt & Durbin 1999; Adrian *et al.* 2000*b*) and have been used to help separate UMZs (Eisma *et al.* 2015), high-shear zones do not typically span the entire domain or provide a complete zonal separation of the flow. We thus conduct our comparison of domain-separating MTBs with other level-sets that span the domain. We also include in this comparison the NTSE field.

Figure 12(*a*) shows the TSE values calculated for initial conditions on the $z = 2.75h$ plane with the interface drawn in blue. The interface effectively contours around the outside of a strongly stretching spiral feature and separates the flow into a less turbulent and more turbulent region. The NTSE field in figure 12(*b*) reveals many of the same structures tangent to the MTB with additional weaker features aligned above the interface. Slight differences between contours in TSE and NTSE fields on the edge of the domain can be attributed to fixed time step integration effects.

Figure 12(*d*) shows the streamwise velocity, a scalar field whose contours are broadly used for extraction of uniform momentum zones in wall turbulence (e.g. Adrian *et al.* 2000*b*; Kwon *et al.* 2014; De Silva *et al.* 2015). Following the procedure of Kwon *et al.* (2014), we have normalized the velocities by the channel centreline velocity. We note that the predominant gradient in the velocity field follows approximately through the centre of the vortical feature, and the velocity contours are parallel with the MTB in only a small region of the domain. We will further explore the differences between UMZ interfaces MTB interfaces below.

Lastly, figure 12(*c*) shows the vorticity norm in the same domain, a diagnostic commonly used in TNTI identification (see Holzner *et al.* 2006; Da Silva *et al.* 2014). This plot provides a similar but simpler picture of the flow dynamics in comparison with TSE, but the details do not indicate exactly where an interface should be drawn. There is no localized shear-driven vorticity peak along the turbulent interface, as is sometimes possible at the TNTI (Da Silva *et al.* 2014). Additionally, the change in vorticity is quite gradual, not giving a clear jump in the vorticity p.d.f. as is often used to separate rotational and irrotational flow fields. For these reasons, vorticity is not commonly used for internal interface diagnostics, but is included here as it does provide a closer comparison with momentum barrier field behaviour than the streamwise velocity (UMZ) visualization. As well, much of UMZ theory relies on an analogy with jumps across turbulent/non-turbulent interfaces.

The ability of the TSE field to identify divergent behaviour of barrier streamlines and appropriately locate the MTB is illustrated in figure 13. Here, we expand our focus from figure 12 to a narrow subsection of the channel. Figure 13(*a,c*) shows the local geometry of

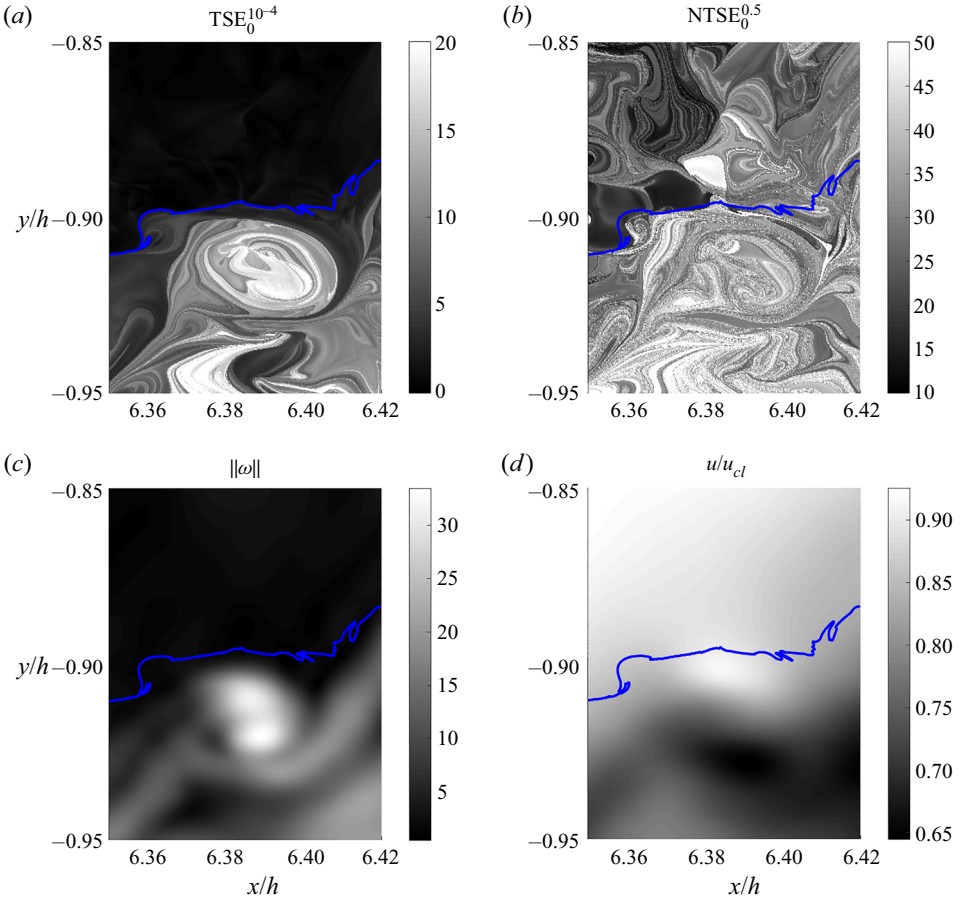

Figure 12. CW from: (*a*) the TSE field; (*b*) the NTSE field for the unit barrier field; (*c*) the vorticity norm $\|\boldsymbol{\omega}\|$; and (*d*) the streamwise velocity u normalized by the centreline velocity u_{cl}. The MTB interface is superimposed in all plots as a blue curve. All image data are computed and displayed at the same spatial resolution.

the MTB (blue) and UMZ (red) interfaces near the $z = 2.75$ plane. Figure 13(*b,d*) shows a zoomed in view of the interfaces in the domain of figure 12 and the nearby trajectories of the barrier equation (2.10).

Trajectories are shaded by their TSE values. For the MTB interface, there is an obvious separation of minimally stretching black trajectories in a less turbulent region above the blue interface and the multiple spiralling grey and white vortices below the interface. The MTB is also tangent to the barrier field streamlines, indicating the correct orientation with respect to the momentum barrier streamsurfaces. This is further confirmed in the inner-product probability distribution inset for the MTB in figure 13(*a,c*). Similar to the findings for TRA level-surfaces around vortices in figure 8, the geometry of TSE level-surface interfaces is largely tangent to perfectly computed zero-flux linear momentum barriers.

The figure 13(*c*) shows the universal $u/u_{cl} = 0.95$ 'quiescent core' UMZ interface calculated over the $1.2h$ streamwise extent, as suggested by Kwon *et al.* (2014). The MTB and UMZ interfaces differ greatly, but the UMZ interface does hint at being influenced by the TSE contours on the right side of the domain. This can be seen in the inner-product

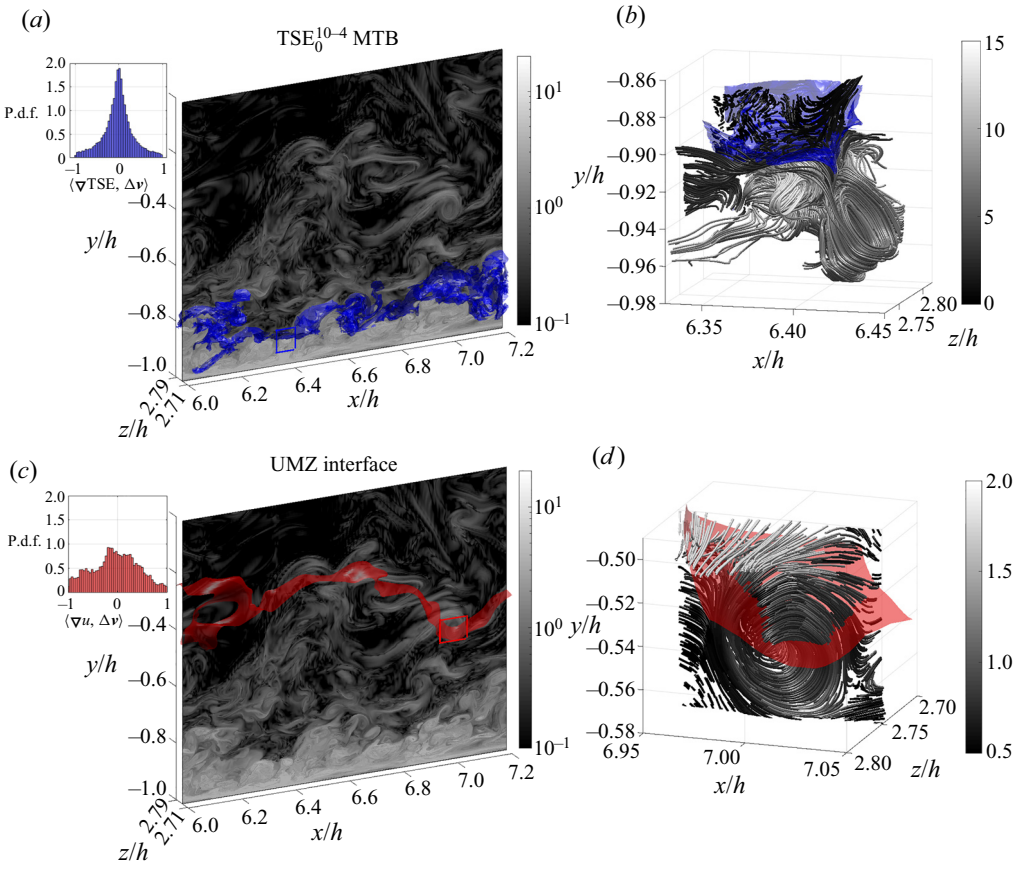

Figure 13. (*a*) TSE field and MTB interface. (*c*) TSE field and UMZ interface. (*b*,*d*) Corresponding interfaces and linear momentum barrier field trajectories coloured by TSE. Inset in each plot are the corresponding p.d.f.s of surface normal innerproducts with the barrier field indicating improved momentum transport limiting abilities of the MTB.

p.d.f. on the left with one such highlighted example shown in Figure 13(*d*). The tangency p.d.f. for the UMZ shows a slight peak around zero corresponding to near parallel points on the right side of the domain. Barrier field streamlines around a vortex feature, however, are seen to be perpendicular to the UMZ interface, thus maximizing transport. This is in direct contrast with our automated MTB interface algorithm that has clearly succeeded in approximating a repelling (and hence structurally stable) invariant manifold of the incompressible barrier equation. Of note, the UMZ interface transects the vortex core, as also seen by velocity contours in figure 12. The UMZ interface is clearly not an organizing structure that blocks momentum transport, but these TSE fields and MTB may begin to give insight into the physical origins of the commonly seen statistical signatures that have supported the ubiquitous use of velocity isosurfaces.

While TSE level surfaces that span the domain at the height of the UMZ do exist, the nearby TSE structures contour and fold around many hyperbolic and elliptic barriers (such as those seen in figure 2) and do not provide a clear interface between distinct wall-parallel flow zones. We suspect that, in the neighbourhood of the quiescent core interface, a simple quasi-planar structure that blocks wall-transverse momentum flux may not actually exist as the elliptic and hyperbolic barrier field manifolds are less densely concentrated.

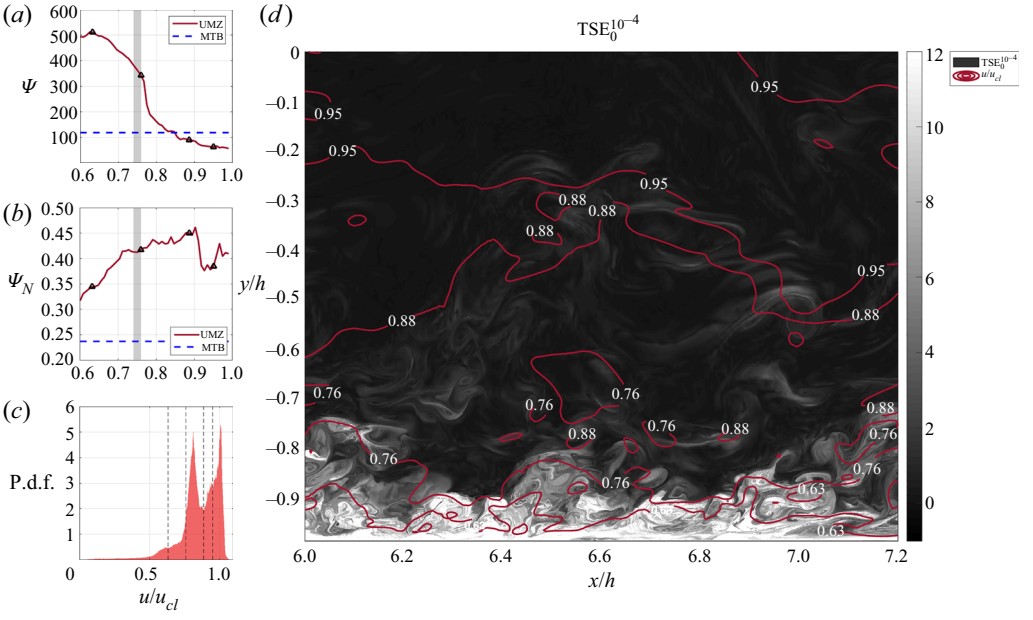

Figure 14. (*a*) Surface-area normalized instantaneous viscous momentum flux Ψ through streamwise velocity isosurfaces (UMZ interfaces). (*b*) Ψ in unit barrier field for streamwise velocity isosurfaces. (*c*) P.d.f. of u/u_{cl}. (*d*) u/u_{cl} contours (with their values indicated) superimposed in red over the TSE field in the $z = 2.75$ plane.

The transverse intersections of velocity level surfaces with invariant manifolds of (2.10) in the p.d.f. of figure 13 suggest any possible correlations between velocity level surfaces and true momentum barriers are insignificant for predictive ability.

To assess this relationship more broadly, we compare the momentum transport through a range of UMZ interfaces and the MTB in figure 14. Figure 14(*d*) shows the same TSE field for the $z = 2.75h$ plane as in figure 12 with overlaid streamwise velocity contours. As there are numerous approaches to extracting the best high-shear streamwise velocity isosurface for UMZ identification (see, e.g. De Silva *et al.* 2015; Fan *et al.* 2019), we directly compare our MTB with a range of simply connected velocity level surfaces from the near-wall region well into the channel core. Figure 14(*a*) shows the geometric diffusive flux across this range of interfaces in red, and our MTB flux in blue. The grey shading indicates the u/u_{cl} isosurfaces closest to the MTB in the domain. As with the non-objective diagnostics in § 3.2, these velocity isosurfaces exhibit around four times the flux as our nearby objective MTB.

As we increase the velocity of the UMZ interface, we also move away from the wall and into a region with smaller $\Delta \boldsymbol{v}$ vectors. While we have seen that the quiescent core UMZ interface is largely transverse to momentum transport barriers, its diffusive momentum flux is smaller than for our MTB. We believe this is due to its location in a region with less turbulence and less flux, and not an ability to limit momentum transport. We thus calculate the normalized geometric flux (tangency measure) Ψ_N from (2.12). In figure 14(*b*), we present Ψ_N for the same UMZ candidates. This shows the clear advantage of identifying internal momentum blocking interfaces with the MTB approach over any streamwise velocity isosurface. Triangles in the two flux plots mark several velocity isosurfaces of interest: the highest flux (0.63), the UMZ closest to the MTB (0.76), the trough between the two p.d.f. peaks (0.88) and the quiescent core UMZ of Kwon *et al.* (2014) (0.95).

The intersection of these four u/u_{cl} isosurfaces with the $z = 2.75h$ plane are drawn in figure 14(*d*).

UMZ theory suggests that momentum is organized into zonal-like structures inside of which there is relatively uniform momentum. These zones are separated by thin viscous shear layers that are often thought to concentrate spanwise vorticity (Meinhart & Adrian 1995). Transport of momentum is concentrated to the viscous-inertial layers which separate the zones with the interfaces between them identifiable from streamwise velocity histograms. Whether in boundary layers or channel flows, UMZ interfaces have been defined as minima between peaks in the p.d.f. for u and correlated with high-shear. Figure 14(*c*) shows a p.d.f. for the bottom half of the channel flow over the 3-D domain of focus. These p.d.f.s are known to be highly sensitive to the size and location of the domain of investigation but there is no consensus available on their use in 2-D or 3-D analysis (Fan *et al.* 2019). The level set values contoured in figure 14(*d*) are marked on the p.d.f. with dashed lines.

It can be seen in figure 14 that streamwise velocity contour interfaces with relatively low diffusive momentum flux do not correspond with momentum transport limiting structures. Indeed, all u/u_{cl} interfaces travel transverse to multiple vortex cores (including that highlighted in figure 13) and meander in and out of high stretching regions. In the Ψ and Ψ_N plots, we can see the surface derived from the minima between the two largest p.d.f. peaks, $u/u_{cl} = 0.88$, does not provide an even locally minimal momentum flux as has been suggested. The steady increase in Ψ_N and decrease in Ψ for increasing u shows the dominant influence of barrier field magnitude on Ψ and a lack of momentum barrier tangency. In fact, the spanning velocity level surface with minimum momentum flux occurs at $u/u_{cl} = 0.99$, which is well inside the less turbulent region of the flow. Of note, the quiescent core, $u/u_{cl} = 0.95$, interface does indeed appear adjacent to the dominant channel core p.d.f. peak, as suggested by Kwon *et al.* (2014). However, the Ψ and Ψ_N and plots show no indication of significant momentum transport organizing structures and no indication that velocity isosurfaces exist inside or on the border of a momentum-organizing zonal-structure. That is, there is no evidence of shear layers of localized vorticity that concentrate or minimize momentum transport between UMZs.

Each panel in figure 15 shows the normalized inner product of respective isosurface normals with the momentum barrier field vector $\Delta \boldsymbol{v}$. As before, values around zero in the p.d.f.s indicate an alignment of isosurfaces with true streamsurfaces of the momentum barrier equation. Figure 15(*a*) shows a familiar peak around 0 for the MTB interface, confirming that the low momentum flux calculated across this interface is aided by its close alignment with a set of invariant manifolds of the barrier equation. There are impressively few isonormal vectors lying outside this peak even with the algorithm balancing strict coincidence invariance under the barrier equation with computational simplicity and moderate curvature.

In comparison, the p.d.f. associated with the closest candidate UMZ interface to the MTB, $u/u_{cl} = 0.76$, exhibits a subtle but much less pronounced peak around zero. Note that this surfaces experiences more than three times the momentum flux across it than the MTB interface. The other two velocity isosurfaces, including the quiescent cored interface, exhibit similar minor peaks around zero, with much more uniform and random alignment of surface normals when compared with the momentum barrier field vectors. This confirms our previous suspicion that flux is primarily minimized across this surface because of its location in a less turbulent region of the flow, and not because it behaves as a physically significant barrier. This is somewhat unsurprising as a simple wall-parallel plane in the neighbourhood of the $u/u_{cl} = 0.95$ level surface has a lower geometric

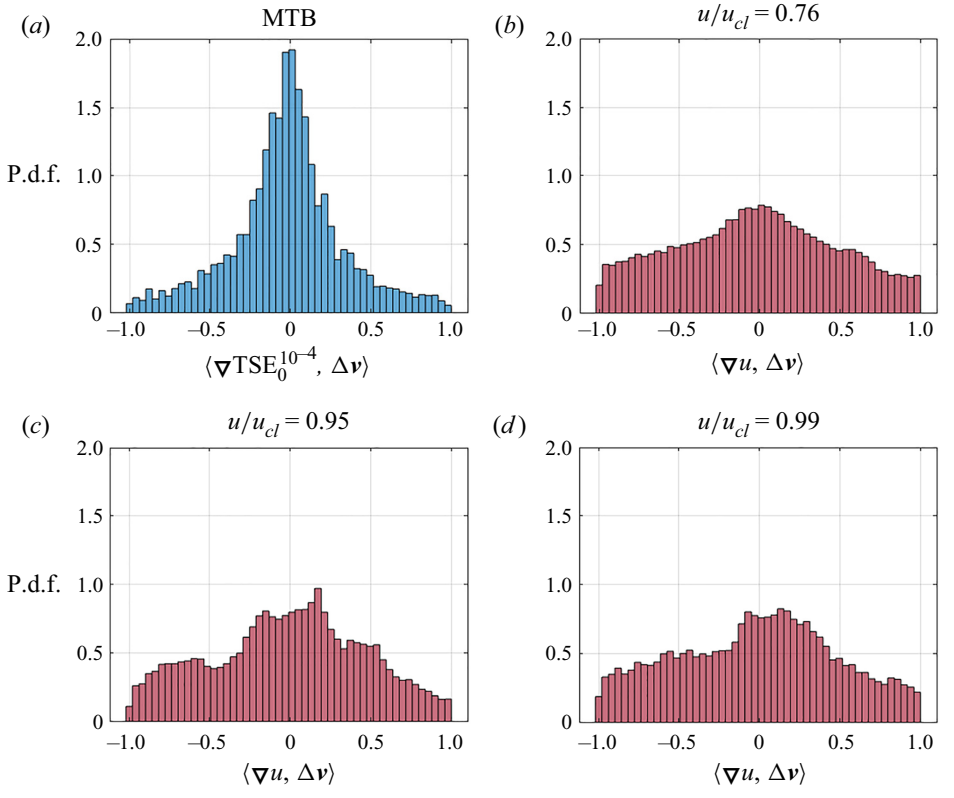

Figure 15. Probability distributions of the normalized inner product of the momentum barrier field vector, $\Delta \boldsymbol{v}$, and the isosurface normals for MTB and UMZ interfaces. There remains a clear singular peak around 0 in the TSE p.d.f., indicating strong agreement between TSE surfaces and the underlying momentum transport blocking interfaces both for vortices and for the connecting regions between them. In contrast, there is significantly more momentum transport across UMZ interfaces.

objective momentum flux than the quiescent core boundary. However, for each contour $u/u_{cl} = 0.76$, 0.88 and 0.95, there are small sections of near tangency with the underlying momentum barriers. While velocity contours and momentum barriers are clearly not equivalent, this again suggests that the method of momentum barrier identification is likely a beneficial avenue for investigating statistical signatures.

We have found the diffusive momentum transport blocking abilities of MTBs in the momentum barrier fields to be consistent in time frames spanning the entire DNS simulations. Focusing on $1.2h \times 0.5h \times 0.2h$ domains, we calculated the TSE fields for 25 frames, generating more than 100 GB of TSE data. The p.d.f. of normalized flux angles consistently follows similar behaviour to that seen figure 14, with an effective approximation to underlying invariant manifolds of the barrier equations.

3.4. *Tracking features and temporal statistics*

The JHTDB $Re = 1000$ channel flow spans 4000 flow-through times (δt). We evaluated the frequency and recurrence of momentum-blocking vortex cores and MTBs in 100 frames with temporal spacing of $40\delta t$ spanning the entire available simulation time. Each frame is adjacent to the lower channel boundary, spanning $h \times 8h$ in the streamwise-wall-normal plane. This required analysing 800 GB of velocity data, and resulted in 30 GB of TRA

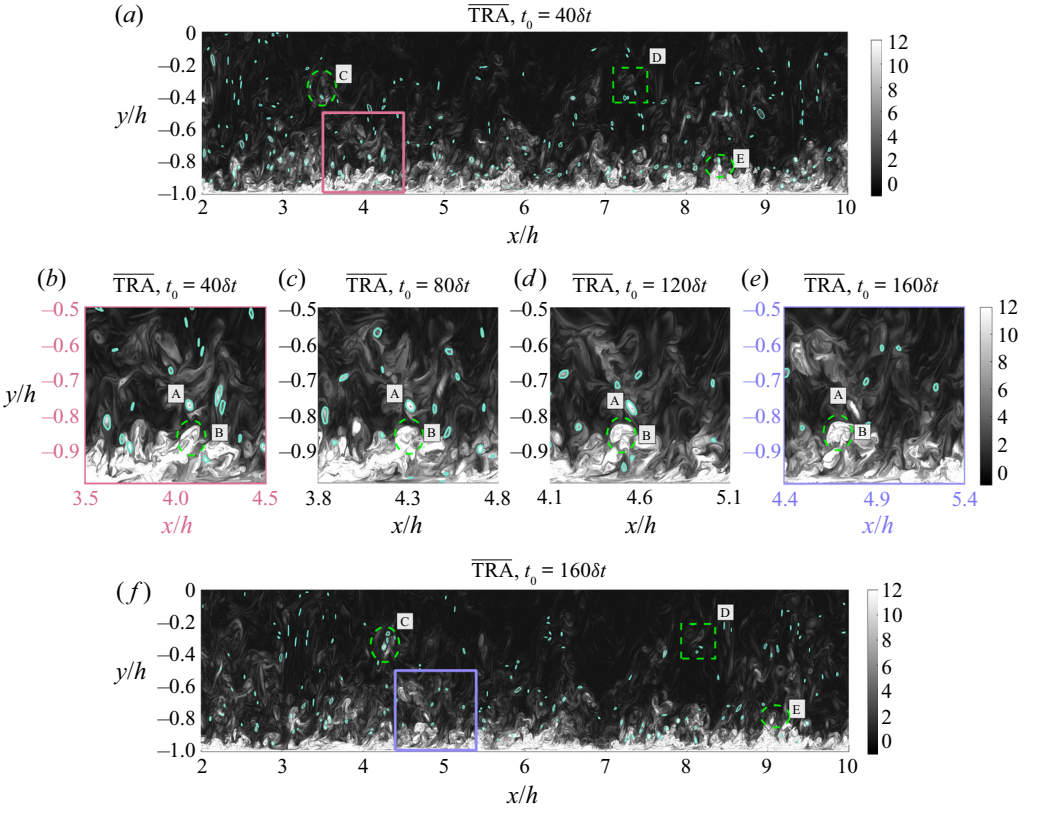

Figure 16. Subsequent $\overline{\text{TRA}}$ fields in the x–z plane spanning 120 channel flow-through times. Multiple features that can be tracked throughout the frames have been identified, with a zoom section and intermediate frames shown in the middle plots. Vortex boundaries identified as the outermost closed $\overline{\text{TRA}}$ contours are also drawn, many of which can be tracked between frames.

and TSE fields, which are available at https://doi.org/10.3929/ethz-b-000541784, as is an animation of the time evolution of TSE frames in the supplementary material at https://doi.org/10.1017/jfm.2022.316.

A visual inspection of subsequent TRA and TSE fields reveals that many easily identifiable Eulerian features remain coherent during fluid advection and can be tracked from one frame to the next. One such example of this feature tracking is shown for the $z = 3h$ plane in figure 16. Figure 16(a,f) plots show TRA fields at $t_0 = 40\delta t$ and $t_0 = 160\delta t$, with figure 16(b–e) tracking features in zoomed areas for intermediate time steps. Some features of interest are labelled A–E; individual vortex cores following Algorithm 1 are highlighted in turquoise.

The vortex immediately to the right of the label A in figure 16(b–e) can be followed from $40\delta t$ to $160\delta t$, though the vortex eventually moves out of frame so that a circular contour is no longer extracted at $160\delta t$. The region labelled B is a cluster of tangled vortices near the top of a wall-connected bulge that is moving away from the wall. Because of the detail possible with TRA, individual components of B can be distinguished and followed between adjacent frames. From $40\delta t$ to $160\delta t$, vortices A and B remain identifiable while being advected nearly a full channel half-width down the channel.

In the wide-views in figure 16(a,f), three additional features are identified and tracked. There are two vortex clusters, C and D, sitting approximately $0.7h$ from the wall in a much

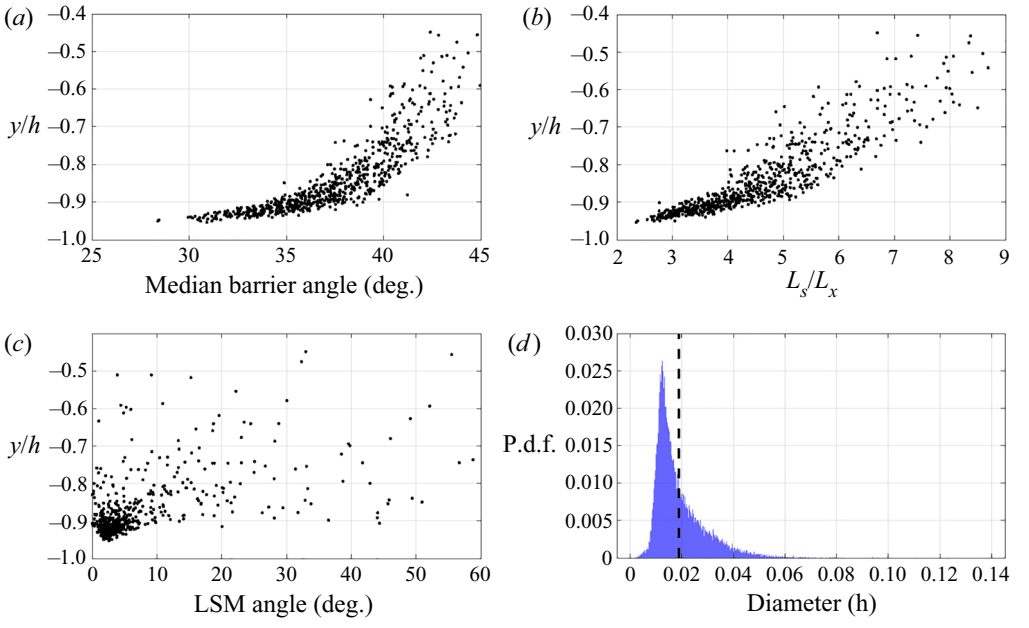

Figure 17. Interface angles and radii of vortex cores (heads) in 3-D frames spanning 4000 flow-through times.

faster moving part of the channel. Vortex E is also tracked as the uppermost vortex on a bulge that has migrated approximately $0.75h$ down the channel. Note that the advection velocity of these five features is fairly consistent though their wall-normal locations vary by $0.6h$. The visual matching of these features was verified by advecting fluid particles in the DNS velocity field over this time window. While there was some minimal deformation of vortices over the period (not displayed), the advected structures and latter Eulerian detections indeed matched. This is promising for not only Eulerian studies of boundary layer structure evolution in great detail, but also the possible use of material momentum barriers from the Lagrangian theory of Haller *et al.* (2020). A video animation of the TRA fields in this plane spanning the entire DNS database can be found in the supplementary movie.

By statistically analysing the entire temporal extent of the channel flow simulation, we found similar behaviour and characteristics for vortices and MTBs. We analysed all TSE contours that spanned the $8h$ domain and found at least one such contour existed in each frame. The total number identified depends on the choice of the number of contour values to extract. At this Reynolds number, these contours were typically closely adjacent, as in figure 10, though more distinct layering is likely at higher Re, as noted by De Silva *et al.* (2017). We include all TSE contours in our statistical analysis as candidate MTBs in light of potential advances in selection criteria and find this does not skew our statistics or introduce outliers. The median positive angle of each MTB was calculated and is displayed with respect to the median height of that momentum interface in figure 17(*a*). TSE contours follow the boundary of individual vortices and provide a measure of the incline angle of individual hairpins or typical eddies as a function of height. We find growth away from the wall in a similar fashion to existing attached eddy (hairpin vortex packet) models with angles ranging from 30° up to 45° further from the wall (Marusic 2001).

Next, we measured the unit length per streamwise distance (L_s/L_x) of MTBs, similar to Chauhan *et al.* (2014) and De Silva *et al.* (2017). In figure 17(*b*), there is a clear increasing

trend for barriers further from the wall. This agrees with the assessment in previous studies that, at greater distances from the wall, larger scale bulges and valleys contribute to greater L_s/L_x (Townsend 1976; Perry & Chong 1982; Adrian *et al.* 2000*b*; De Silva *et al.* 2017). The L_s/L_x for our MTB exceeds the range of De Silva *et al.* (2017) (< 3), but our mean, $\langle L_s/L_x \rangle = 5.4$, is much closer to that found by Chauhan *et al.* (2014) for the TNTI. This is likely attributed both to physical differences as well as the greater detail and meandering stream-surfaces found in $\Delta \boldsymbol{v}$ when compared to the underlying velocity grid (e.g. figure 2).

By identifying the outermost closed and convex TRA contours, we found momentum vortices which have a mean diameter of $0.019h$. The p.d.f. of this diameter distribution is shown in figure 17(*d*) with the mean marked as a dashed line. These vortex cores are smaller in diameter than the observed tracer eddies of Falco (1974, 1977), and slightly smaller than the $0.03-0.05\delta$ vortex heads identified by Adrian *et al.* (2000*b*). There are several possible reasons for this, the most probable being that the core vortical structure is smaller than its visible influence on the material (and velocity) field. We are restricting to closed and convex contours and thus eliminate the filamentation seen in smoke experiments.

Another commonly referenced statistic in the boundary layer literature is the inclination angle, α, that the envelope of packets of vortices make with the wall, also known as the structure angle or ramp angle. This has been frequently measured by two-point correlations, with limited guidance for quantifying spatially resolved structures beyond the Radon transform used by Hommema & Adrian (2003). We opt to measure the inclination angle of $0.6h$-streamwise-length linear segments that fit our contours of interest with r.m.s. < 0.02, the average diameter of our vortices. This length was chosen as it is less than the lower bound of the streamwise length of bulges reported in the literature and approximately one half the streamwise extent necessary for converged channel flow UMZ statistics (Kwon *et al.* 2014). This provides sufficient streamwise range to find a good linear fit to a ramp without fitting to the small individual sub-components or the large-scale motions. An example of a successful linear fitting is shown in figure 10.

The average α value is found to be 8° with the average ramp centre approximately $0.18h$ away from the wall. There were approximately 75 % as many ramps identified as total number of MTBs. While these angles and heights are similar to the observations of Head & Bandyopadhyay (1981) and seminal UMZ work (see, e.g. Adrian *et al.* 2000*b*), there is significant scatter around these values as can be seen in figure 17(*c*). This suggest the linear fit method should be refined further in future momentum barrier investigations.

4. Conclusions

Using the objective notion of diffusive momentum flux through a material surface, we have developed an algorithm for locating frame-invariant instantaneous barriers to linear momentum transport in near-wall turbulence. This algorithm builds on the recent theory of active transport barriers (Haller *et al.* 2020), which identifies momentum transport barriers as structurally stable invariant manifolds (stream surfaces) of the incompressible steady barrier equation (2.10). Our algorithms extract these invariant manifolds directly and approximate them by level surfaces of recently developed coherent structure diagnostics, the trajectory rotation average (TRA) and trajectory stretching exponent (TSE) proposed by Haller *et al.* (2021). Other objective LCS diagnostics can also be used to identify invariant manifolds of (2.10), but TRA and TSE were used here due to their computational simplicity as single-trajectory-based diagnostic fields and their ability to designate clean boundaries. We also introduce the normalized NTRA and NTSE, which provide

unprecedented detail for coherent structures, with equal fidelity in highly turbulent and less turbulent zones.

Our procedure targets both momentum-trapping vortices in the boundary layer and internal momentum-flux minimizing interfaces that locally define the flow into near-wall and far-from-wall layers. Specifically, vortex boundaries are identified as the outermost cylindrical level surfaces of the TRA field. This procedure is free from the empirical threshold values employed by classic, velocity-gradient-based vortex criteria which provide observer-dependent results. In addition, we find that while classic vortex identification diagnostics can suggest vortices in the neighbourhood of these momentum-blocking vortices, this similarity is without predictive value and fails to generate surfaces that sufficiently block momentum transport. We believe that the underlying momentum-blocking structures are influencing the gradient-based diagnostics, but the classic diagnostics cannot be used as a proxy measure as they maintain no predictive physical (transport-limiting) value.

The same barrier field trajectory data can also be used to compute TSE fields and identify wall-parallel quasi-planar momentum transport barrier (MTB) interfaces that locally minimize the diffusive transport of momentum. With TRA and TSE fields, the diffusive linear momentum barrier vector field (2.10) therefore links vortex diagnostics with internal fluid interfaces, as seen in tracer field observations, and are objective analogues of the broadly used but frame-dependent UMZ interfaces and TNTIs. We have found that MTB interfaces significantly outperform the classic UMZ interface approaches, in terms of their ability to block viscous momentum transport, regardless of the specific velocity chosen. The use of TSE calculations for the barrier equations eliminates sensitivities in UMZ analysis with respect to changes in the number of bins used in velocity histograms and variations in the size of the domain of analysis. In comparison, the only free parameter in our vortex and MTB algorithm is the spatial resolution of TSE fields, although this is simply a question of computational resources. Whereas increases in spatial resolution reduce momentum transport through vortex and MTB extractions, increases in the number of velocity histogram bins eventually lead to the disappearance of any UMZ peak or interface.

This first-principles approach of starting with an objective momentum flux provides universal diagnostics based on physics for future structure extraction techniques, the Ψ and Ψ_N fields. Furthermore, the objective nature of this work provides frame-indifferent structures that are experimentally verifiable (e.g. Eisma *et al.* 2021), unlike the predictions from non-objective criteria. The vortices and MTB identified are resilient under fluid advection, providing a new way in which to track the evolution of individual or clusters of structures. In this way, we hope to provide a common test to verify models and settle longstanding debates in fluids, such as the prevalence or importance of hairpin structures in the boundary layer (see, e.g. Marusic & Monty 2019), and the role of inner versus outer layer motions.

Techniques for three-component PIV measurements are rapidly advancing (Raffel *et al.* 2018), and the momentum-transport barrier techniques examined here provide a new way to identify such barriers in an observer-independent fashion in the same flow volume as these data increase in ubiquity. For experimental flows in which volumes of 3-D measurements are not available, there is also potential for developing symmetry arguments, such as those provided by Haller *et al.* (2020). These can, for instance, simplify the barrier vector field to fewer components for flows with strong anisotropy. Qualitative comparisons between structures in numerical simulations and tracer experiments may also provide insights by determining the roles of analogous features when experimental velocity measurements are unavailable.

Future research should investigate the role that parabolic invariant manifolds of the momentum barrier equation (2.10) play in near-wall turbulence as well. Haller *et al.* (2020) also derive a barrier equation for the transport of vorticity, which takes the form $\boldsymbol{x}' = \Delta\boldsymbol{\omega}$. The streamsurfaces of the latter barrier equation generally differ from those of (2.10) and hence would highlight different internal interfaces in near-wall turbulence in a theory that seeks vorticity transport minimizing interfaces. Another extension of the present theory could use the Lagrangian active barriers introduced in Haller *et al.* (2020), which are material surfaces minimizing momentum or vorticity transport over a whole time interval rather than just instantaneously. Such material barriers should mimic the structures seen in the classic smoke experiments of Falco (1977) even more closely.

Supplementary movie. Supplementary movie is available at https://doi.org/10.1017/jfm.2022.316.

Acknowledgements. The Johns Hopkins Turbulence Database used in this study is accessible at https://doi.org/10.7281/T10K26QW.

Funding. The authors acknowledge financial support from Priority Program SPP 1881 (Turbulent Superstructures) of the German National Science Foundation (DFG) and the Swiss National Science Foundation (SNSF) Postdoc Mobility Fellowship Project P400P2 199190.

Declaration of interests. The authors report no conflict of interest.

Author ORCIDs.
Nikolas O. Aksamit https://orcid.org/0000-0002-2610-7258;
George Haller https://orcid.org/0000-0003-1260-877X.

Appendix A. Total objective momentum flux

For the unsteady ABC flow

$$\boldsymbol{v}(\boldsymbol{x}, t) = e^{-\nu t}\boldsymbol{v}^0(\boldsymbol{x}), \quad \boldsymbol{v}^0(\boldsymbol{x}) = \begin{pmatrix} A\sin x_3 + C\cos x_2 \\ B\sin x_1 + A\cos x_3 \\ C\sin x_2 + B\cos x_1 \end{pmatrix}, \tag{A1a,b}$$

Theorem 7.5 of Haller *et al.* (2020) guarantees that the instantaneous barriers to diffusive momentum transport coincide with the structurally stable 2-D invariant manifolds of the flow generated by the steady velocity field $\boldsymbol{v}^0$, as well as the material and instantaneous barriers to vorticity transport. Specifically, the Eulerian barrier equation for momentum transport is

$$\boldsymbol{x}' = \nu\rho\Delta\boldsymbol{v} = -\nu\rho k^2\alpha(t)\boldsymbol{v}^0(\boldsymbol{x}). \tag{A2}$$

Note that

$$\boldsymbol{v}_t = -\nu\boldsymbol{v}^0(\boldsymbol{x}), \quad \nu\Delta\boldsymbol{v} = -\nu\boldsymbol{v}^0(\boldsymbol{x}), \tag{A3a,b}$$

where the second identity follows from the Beltrami property with $k = 1$ in this case. Therefore, using the Navier–Stokes equations, we obtain

$$-\frac{1}{\rho}\nabla p = (\nabla\boldsymbol{v})\,\boldsymbol{v} = \begin{pmatrix} 0 & -C\sin x_2 & A\cos x_3 \\ B\cos x_1 & 0 & -A\sin x_3 \\ -B\sin x_1 & C\cos x_2 & 0 \end{pmatrix}\begin{pmatrix} A\sin x_3 + C\cos x_2 \\ B\sin x_1 + A\cos x_3 \\ C\sin x_2 + B\cos x_1 \end{pmatrix}$$
$$= \begin{pmatrix} -BC\sin x_1\sin x_2 + AB\cos x_1\cos x_3 \\ BC\cos x_1\cos x_2 - AC\sin x_2\sin x_3 \\ -AB\sin x_1\sin x_3 + AC\cos x_2\cos x_3 \end{pmatrix} \tag{A4}$$

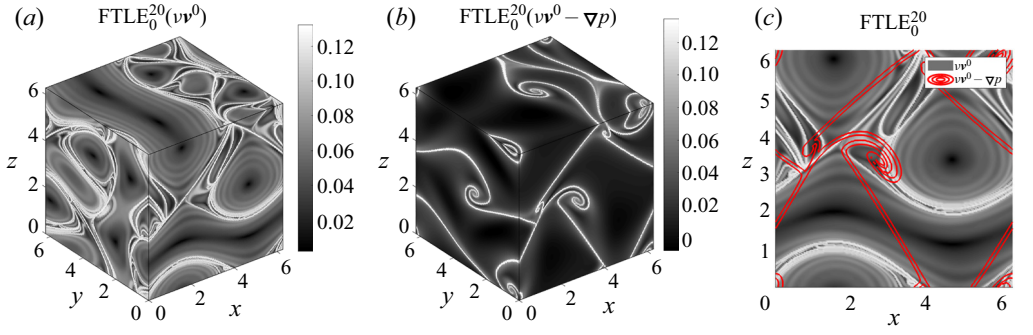

Figure 18. Comparison of structurally stable transport barriers as identified by FTLE. (*a*) Barriers to diffusive momentum flux. (*b*) Barriers to total momentum flux after including the pressure gradient. (*c*) Comparison of diffusive and total momentum barriers on the $y = 2\pi$ plane.

The pressure gradient, therefore, has a different magnitude and orientation relative to $\Delta\boldsymbol{v} = \boldsymbol{v}^0$. This discrepancy can indeed be seen in figure 18 where the FTLE field is calculated for $\Delta\boldsymbol{v}$ and (A4).

We note that for the turbulent channel flow of focus here, the streamwise velocity gradient is predominantly orthogonal to the pressure gradient. Thus, the shear interfaces used to delineate uniform momentum zones actually maximize the total momentum transport through them.

Following these discussions and the connections drawn between momentum zones and experimentally observable barriers (Westerweel *et al.* 2009), we find that our definition of active transport that focuses on surfaces that block the viscous transport (as opposed to the total transport) of momentum and vorticity is the correct one for the purposes of structure identification that is experimentally reproducible.

References

Adrian, R.J. 2007 Hairpin vortex organization in wall turbulence. *Phys. Fluids* **19** (4), 041301.

Adrian, R.J., Christensen, K.T. & Liu, Z.C. 2000*a* Analysis and interpretation of instantaneous turbulent velocity fields. *Exp. Fluids* **29** (3), 275–290.

Adrian, R.J., Meinhart, C.D. & Tomkins, C.D. 2000*b* Vortex organization in the outer region of the turbulent boundary layer. *J. Fluid Mech.* **422**, 1–54.

Astarita, G. 1979 Objective and generally applicable criteria for flow classification. *J. Non-Newtonian Fluid Mech.* **6** (1), 69–76.

Bandyopadhyay, P. 1980 Large structure with a characteristic upstream interface in turbulent boundary layers. *Phys. Fluids* **23** (11), 2326–2327.

Bautista, J.C.C., Ebadi, A., White, C.M., Chini, G.P. & Klewicki, J.C. 2019 A uniform momentum zone-vortical fissure model of the turbulent boundary layer. *J. Fluid Mech.* **858**, 609–633.

Beron-Vera, F.J., Hadjighasem, A., Xia, Q., Olascoaga, M.J. & Haller, G. 2018 Coherent Lagrangian swirls among submesoscale motions. *Proc. Natl Acad. Sci.* **116** (37), 201701392.

Chauhan, K., Philip, J., De Silva, C.M., Hutchins, N. & Marusic, I. 2014 The turbulent/non-turbulent interface and entrainment in a boundary layer. *J. Fluid Mech.* **742**, 119–151.

Da Silva, C.B., Hunt, J.C.R., Eames, I. & Westerweel, J. 2014 Interfacial layers between regions of different turbulence intensity. *Annu. Rev. Fluid Mech.* **46** (1), 567–590.

De Silva, C.M., Hutchins, N. & Marusic, I. 2015 Uniform momentum zones in turbulent boundary layers. *J. Fluid Mech.* **786**, 309–331.

De Silva, C.M., Philip, J., Hutchins, N. & Marusic, I. 2017 Interfaces of uniform momentum zones in turbulent boundary layers. *J. Fluid Mech.* **820**, 451–478.

Dennis, D.J.C. & Nickels, T.B. 2011 Experimental measurement of large-scale three-dimensional structures in a turbulent boundary layer. Part 1. Vortex packets. *J. Fluid Mech.* **673**, 180–217.

DONG, Y. & TIAN, W. 2020 On the thresholds of vortex visualisation methods. *Intl J. Comput. Fluid Dyn.* **34** (4), 267–277.

DROUOT, R. 1976 Definition d'un transport associe un modele de fluide de deuxieme ordre. *C. R. Acad. Sci. Pari* A **282**, 923–926.

DROUOT, R. & LUCIUS, M. 1976 Approximation du second ordre de la loi de comportement des fluides simples. Lois classiques deduites de l'introduction d'un nouveau tenseur objectif. *Arch. Mech. Stos.* **28** (2), 189–198.

DUBIEF, Y. & DELCAYRE, F. 2000 On coherent-vortex identification in turbulence. *J. Turbul.* **1**, N11.

EISMA, J., WESTERWEEL, J., OOMS, G. & ELSINGA, G.E. 2015 Interfaces and internal layers in a turbulent boundary layer. *Phys. Fluids* **27**, 055103.

EISMA, J., WESTERWEEL, J. & VAN DE WATER, W. 2021 Do coherent structures organize scalar mixing in a turbulent boundary layer? *J. Fluid Mech.* **929**, A14.

EYINK, G.L., GUPTA, A. & ZAKI, T.A. 2020 Stochastic Lagrangian dynamics of vorticity. Part 2. Application to near-wall channel-flow turbulence. *J. Fluid Mech.* **901**, A3.

FALCO, R. 1974 Some comments on turbulent boundary layer structure inferred from the movements of a passive contaminant. In *AIAA 12th Aerospace Science Meeting, AIAA Paper* 1974–99.

FALCO, R.E. 1977 Coherent motions in the outer region of turbulent boundary layers. *Phys. Fluids* **20** (10), S124.

FAN, D., XU, J., YAO, M.X. & HICKEY, J.P. 2019 On the detection of internal interfacial layers in turbulent flows. *J. Fluid Mech.* **872**, 198–217.

FARAZMAND, M. & HALLER, G. 2016 Polar rotation angle identifies elliptic islands in unsteady dynamical systems. *Physica* D **315**, 1–12.

FIEDLER, H. & HEAD, M.R. 1966 Intermittency measurements in the turbulent boundary layer. *J. Fluid Mech.* **25** (4), 719–735.

GANAPATHISUBRAMANI, B., LONGMIRE, E.K. & MARUSIC, I. 2006 Experimental investigation of vortex properties in a turbulent boundary layer. *Phys. Fluids* **18** (5), 055105.

GAO, Q., ORTIZ-DUE NS, C. & LONGMIRE, E.K. 2011 Analysis of vortex populations in turbulent wall-bounded flows. *J. Fluid Mech.* **678**, 87–123.

GRAHAM, J., *et al.* 2016 A Web Services-accessible database of turbulent channel flow and its use for testing a new integral wall model for LES. *J. Turbul.* **17** (2), 181–215.

GREEN, M.A., ROWLEY, C.W. & HALLER, G. 2007 Detection of Lagrangian coherent structures in three-dimensional turbulence. *J. Fluid Mech.* **572**, 111–120.

GUL, M., ELSINGA, G.E. & WESTERWEEL, J. 2020 Internal shear layers and edges of unifrom momentum zones in a turbulent pipe flow. *J. Fluid Mech.* **901**, A10.

GÜNTHER, T. & THEISEL, H. 2018 The state of the art in vortex extraction. *Comput. Graph. Forum* **37** (6), 149–173.

HALLER, G. 2005 An objective definition of a vortex. *J. Fluid Mech.* **525**, 1–26.

HALLER, G. 2015 Lagrangian coherent structures. *Annu. Rev. Fluid Mech.* **47**, 137–162.

HALLER, G. 2021 Can vortex criteria be objectivized? *J. Fluid Mech.* **908**, A25.

HALLER, G., AKSAMIT, N. & BARTOS, A.P.E. 2021 Quasi-objective coherent structure diagnostics from single trajectories. *Chaos* **31**, 043131.

HALLER, G., HADJIGHASEM, A., FARAZMAND, M. & HUHN, F. 2016 Defining coherent vortices objectively from the vorticity. *J. Fluid Mech.* **795**, 136–173.

HALLER, G., KARRASCH, D. & KOGELBAUER, F. 2018 Material barriers to diffusive and stochastic transport. *Proc. Natl Acad. Sci.* **115** (37), 9074–9079.

HALLER, G., KATSANOULIS, S., HOLZNER, M., FROHNAPFEL, B. & GATTI, D. 2020 Objective material barriers to the transport of momentum and vorticity. *J. Fluid Mech.* **905**, A17

HE, G.S., PAN, C., FENG, L.H., GAO, Q. & WANG, J.J. 2016 Evolution of Lagrangian coherent structures in a cylinder-wake disturbed flat plate boundary layer. *J. Fluid Mech.* **792**, 274–306.

HEAD, M.R. & BANDYOPADHYAY, P. 1981 New aspects of turbulent boundary-layer structure. *J. Fluid Mech.* **107** (11), 297–338.

HOLZNER, M., LIBERZON, A., GUALA, M., TSINOBER, A. & KINZELBACH, W. 2006 Generalized detection of a turbulent front generated by an oscillating grid. *Exp. Fluids* **41** (5), 711–719.

HOMMEMA, S.E. & ADRIAN, R.J. 2003 Packet structure of surface eddies in the atmospheric boundary layer. *Boundary-Layer Meteorol.* **106** (1), 147–170.

HUNT, J.C.R. & DURBIN, P.A. 1999 Perturbed vortical layers and shear sheltering. *Fluid Dyn. Res.* **24** (6), 375–404.

HUNT, J.C.R., WRAY, A.A. & MOIN, P. 1988 Eddies, streams, and convergence zones in turbulent flows. In *Center for Turbulence Research, Proceedings of the Summer Program*, pp. 193–208.

HWANG, J. & SUNG, H.J. 2018 Wall-attached structures of velocity fluctuations in a turbulent boundary layer. *J. Fluid Mech.* **856**, 958–983.

JEONG, J. & HUSSAIN, F. 1995 On the Identification of a vortex. *J. Fluid Mech.* **285**, 69–94.

JIE, Y., ANDERSSON, H.I. & ZHAO, L. 2021 Effects of the quiescent core in turbulent channel flow on transport and clustering of inertial particles. *Intl J. Multiphase Flow* **140**, 103627.

KIRWAN, A.D. 2016 On objectivity, irreversibility and non-Newtonian fluids. *Fluids* **1** (1), 1–14.

KLINE, S.J., REYNOLDS, W.C., SCHRAUB, F.A. & RUNSTADLER, P.W. 1967 The structure of turbulent boundary layers. *J. Fluid Mech.* **30** (4), 741–773.

KWON, Y.S., HUTCHINS, N. & MONTY, J.P. 2016 On the use of the Reynolds decomposition in the intermittent region of turbulent boundary layers. *J. Fluid Mech.* **794**, 5–16.

KWON, Y.S., PHILIP, J., DE SILVA, C.M., HUTCHINS, N. & MONTY, J.P. 2014 The quiescent core of turbulent channel flow. *J. Fluid Mech.* **751**, 228–254.

LASKARI, A., DE KAT, R., HEARST, R.J. & GANAPATHISUBRAMANI, B. 2018 Time evolution of uniform momentum zones in a turbulent boundary layer. *J. Fluid Mech.* **842**, 554–590.

LI, Y., PERLMAN, E., WAN, M., YANG, Y., BURNS, R., MENEVEAU, C., BURNS, R., CHEN, S., SZALAY, A. & EYINK, G. 2008 A public turbulence database cluster and applications to study Lagrangian evolution of velocity increments in turbulence. *J. Turbul.* **9**, N31.

LIU, J., GAO, Y. & LIU, C. 2019*a* An objective version of the Rortex vector for vortex identification. *Phys. Fluids* **31** (6), 065112.

LIU, J., SHENG GAO, Y., QIAN WANG, Y. & LIU, C. 2019*b* Objective Omega vortex identification method. *J. Hydrodyn.* **31** (3), 455–463.

LUGT, H.J. 1979 The Dilemma of Defining a Vortex. In *Recent Developments in Theoretical and Experimental Fluid Mechanics* (ed. B. Schmidt, U. Müller & K.G. Roesner). Springer.

MARUSIC, I. 2001 On the role of large-scale structures in wall turbulence. *Phys. Fluids* **13** (3), 735–743.

MARUSIC, I. & MONTY, J.P. 2019 Attached eddy model of wall turbulence. *Annu. Rev. Fluid Mech.* **51** (1), 49–74.

MEINHART, C.D. & ADRIAN, R.J. 1995 On the existence of uniform momentum zones in a turbulent boundary layer. *Phys. Fluids* **7** (4), 694–696.

MONTEMURO, B., WHITE, C.M., KLEWICKI, J.C. & CHINI, G.P. 2020 A self-sustaining process theory for uniform momentum zones and internal shear layers in high Reynolds number shear flows. *J. Fluid Mech.* **901**, A28.

NEAMTU-HALIC, M.M., KRUG, D., HALLER, G. & HOLZNER, M. 2019 Lagrangian coherent structures and entrainment near the turbulent/non-Turbulent interface of a gravity current. *J. Fluid Mech.* **877**, 824–843.

OFFEN, G.R. & KLINE, S.J. 1974 Combined dye-streak and hydrogen-bubble visual observations of a turbulent boundary layer. *J. Fluid Mech.* **62** (2), 223–239.

PAN, C., WANG, J.J. & ZHANG, C. 2009 Identification of lagrangian coherent structures in the turbulent boundary layer. *Sci. China* G **52** (2), 248–257.

PEACOCK, T., FROYLAND, G. & HALLER, G. 2015 Introduction to focus issue: objective detection of coherent structures. *Chaos* **25** (8), 087201.

PERLMAN, E., BURNS, R., LI, Y. & MENEVEAU, C. 2007 Data exploration of turbulence simulations using a database cluster. In *Supercomputing SC07*, ACM, IEEE.

PERRY, A.E. & CHONG, M.S. 1982 On the mechanism of wall turbulence. *J. Fluid Mech.* **119**, 173–217.

RAFFEL, M., WILLERT, C.E., SCARANO, F., KÄHLER, C.J., WERELEY, S.T. & KOMPENHANS, J. 2018 Techniques for 3D-PIV. In *Particle Image Velocimetry*, pp. 309–365. Springer.

SAXTON-FOX, T. & MCKEON, B.J. 2017 Coherent structures, uniform momentum zones and the streamwise energy spectrum in wall-bounded turbulent flows. *J. Fluid Mech.* **826**, 1–12.

SERRA, M., SATHE, P., BERON-VERA, F. & HALLER, G. 2017 Uncovering the edge of the polar vortex. *J. Atmos. Sci.* **74** (11), 3871–3885.

SERRA, M., SATHE, P., RYPINA, I., KIRINCICH, A., ROSS, S.D., LERMUSIAUX, P., ALLEN, A., PEACOCK, T. & HALLER, G. 2020 Search and rescue at sea aided by hidden flow structures. *Nat. Commun.* **11** (1), 2525.

TOWNSEND, A.A. 1976 *The Structure of Turbulent Shear Flow*, 2nd edn. Cambridge University Press.

WESTERWEEL, J., FUKUSHIMA, C., PEDERSEN, J.M. & HUNT, J.C.R. 2009 Momentum and scalar transport at the turbulent/non-turbulent interface of a jet. *J. Fluid Mech.* **631**, 199–230.

WILSON, Z.D., TUTKUN, M. & CAL, R.B. 2013 Identification of Lagrangian coherent structures in a turbulent boundary layer. *J. Fluid Mech.* **728**, 396–416.

ZHOU, J., ADRIAN, R.J., BALACHANDAR, S. & KENDALL, T.M. 1999 Mechanisms for generating coherent packets of hairpin vortices in channel flow. *J. Fluid Mech.* **387**, 353–396.